Uncertainty quantification of the multi-centennial response of the Antarctic Ice Sheet to climate change

Kevin Bulthuis[1,2], Maarten Arnst[1], Sainan Sun[2], and Frank Pattyn[2]

[1]Computational and Stochastic Modeling, Aerospace and Mechanical Engineering, Université de Liège, Allée de la Découverte 9, Quartier Polytech 1, 4000 Liège, Belgium
[2]Laboratoire de Glaciologie, Department of Geosciences, Environment and Society, Université Libre de Bruxelles, Av. F.D. Roosevelt 50, 1050 Brussels, Belgium

Correspondence: Kevin Bulthuis (kevin.bulthuis@uliege.be)

Abstract. Ice loss from the Antarctic ice sheet (AIS) is expected to become the major contributor to sea-level rise in the next centuries. Projections of the AIS response to climate change based on numerical ice-sheet models remain challenging to establish due to the complexity of physical processes involved in ice-sheet dynamics, including instability mechanisms that can destabilise marine sectors with retrograde slopes. Moreover, uncertainties in ice-sheet models limit the ability to provide accu-
5 rate sea-level rise projections. Here, we apply probabilistic methods to a hybrid ice-sheet model to investigate the influence of several sources of uncertainty, namely sources of uncertainty in atmospheric forcing, basal sliding, grounding-line flux parameterisation, calving, sub-shelf melting, ice-shelf rheology and bedrock relaxation, on the continental response of the Antarctic ice sheet to climate change over the next millennium. We provide probabilistic projections of sea-level rise and grounding-line retreat and we carry out stochastic sensitivity analyses to determine the most influential sources of uncertainty. We find that all
10 sources of uncertainty, except perhaps the bedrock relaxation times, contribute to the uncertainty in the projections. We show that the sensitivity of the projections to uncertainties increases and the contribution of the uncertainty in sub-shelf melting to the uncertainty in the projections becomes more and more dominant as the scenario gets warmer. We show that the significance of the AIS contribution to sea-level rise is controlled by marine ice-sheet instability (MISI) in marine basins, with the biggest contribution stemming from the more vulnerable West Antarctic ice sheet. We find that, irrespectively of parametric
15 uncertainty, the strongly mitigated RCP 2.6 scenario prevents the collapse of the West Antarctic ice sheet, that in both RCP 4.5 and RCP 6.0 scenarios the occurrence of MISI in marine basins is more sensitive to parametric uncertainty and that, almost irrespectively of parametric uncertainty, RCP 8.5 triggers the collapse of the West Antarctic ice sheet.

Copyright statement. TEXT

1 Introduction

20 The Antarctic ice sheet (AIS) is the largest reservoir of freshwater on Earth (∼60 m sea-level equivalent) and has the potential to become one of the largest contributors to sea-level rise in the next centuries. Yet, the IPCC Fifth Assessment Report (AR5)

(Stocker et al., 2013) has identified the magnitude of the AIS response as the largest source of uncertainty in projecting sea-level rise, when compared with other contributors, such as thermal expansion, glaciers and the Greenland ice sheet. Recent observations (Shepherd et al., 2018) have shown an acceleration in the rate of ice loss from the Antarctic ice sheet, especially in West Antarctica where an irreversible retreat may be underway in the Amundsen Sea embayment as a consequence of a

5 marine ice-sheet instability (MISI) (Favier et al., 2014; Joughin et al., 2014; Rignot et al., 2014).

Assessing the future response of the Antarctic ice sheet requires numerical ice-sheet models amenable to large-scale and long-term simulations and quantification of the impact of modelling hypotheses and parametric uncertainty. So far, there exist only a limited number of projections (Golledge et al., 2015; Ritz et al., 2015; DeConto and Pollard, 2016; Schlegel et al., 2018) for the whole Antarctic ice sheet on a (multi-)centennial time scale. These projections show similar trends for the next

10 centuries, but they differ in the magnitude of the mass loss they predict, with differences and uncertainty ranges that may be of several metres for eustatic sea level. Using a numerical ice-sheet model supplemented with a statistical approach for the probability of MISI onset, Ritz et al. (2015) have projected a contribution to sea-level rise around 0.1 m by 2100 with a very low probability of exceeding 0.5 m in the A1B scenario. Running their simulations with and without sub-grid melt interpolation at the grounding line, Golledge et al. (2015) have projected that sea-level rise could range from 0.01 m to 0.38 m by 2100 and

15 from 0.21 m to more than 5 m by 2500 considering all RCP scenarios. Including the marine ice-cliff instability mechanism (Pollard et al., 2015) in a numerical ice-sheet model, DeConto and Pollard (2016) have projected that sea level could rise much more significantly, with projections exceeding 1 m by 2100 and 15 m by 2500 in the RCP 8.5 scenario.

Despite recent progress in the numerical modelling of ice-sheet dynamics (Pattyn et al., 2017), differences in modelling hypotheses between ice-sheet models remain a major source of uncertainty for sea-level rise projections. Intercomparison

20 projects such as the SeaRise project (Bindschadler et al., 2013) and the ongoing ISMIP6 project (Nowicki et al., 2016; Goelzer et al., 2018) aim at quantifying the impact of such so-called structural uncertainty in ice-sheet models by comparing projections from multiple numerical models. Such multimodel ensembles give some insight into the impact of the structural uncertainty, although challenges remain in combining the different results (Knutti et al., 2010).

Uncertainties in the ice-sheet initial state, climate forcing and parameters in numerical ice-sheet models are another major

25 limitation for accurate projections. To date, the impact of such parametric uncertainty is assessed most often by using large ensemble analysis, that is, the model is run for different values of the parameters and the uncertainty in the projections is estimated from the spread in the model runs. For example, Golledge et al. (2015) ran their model with simplified sensitivity experiments to evaluate qualitatively the sensitivity of the Antarctic ice sheet to temperature, precipitation and sea surface temperature individually, while DeConto and Pollard (2016) assessed the sensitivity of their model to parametric uncertainty

30 by evaluating the model response at a few samples in the parameter space. By contrast, Ritz et al. (2015) adopted a probabilistic approach and estimated the uncertainty in sea-level rise projections by running an ice-sheet model with samples of parameters drawn randomly from probability density functions for the parameters and subsequently deducing probability density functions for sea-level rise projections.

The recently formed uncertainty quantification (UQ) community develops theory and methods to describe quantitatively

35 the origin, propagation and interplay of sources of uncertainty in the analysis and projection of the behaviour of complex

systems in science and engineering; see, for instance, Ghanem et al. (2017) for a recent handbook and Arnst and Ponthot (2014) for a recent review paper. Most of this theory and these methods are based on the probability theory, in the context of which uncertain parameters and projections are represented as random variables characterised by their probability density function. Theory and methods are under development to characterise sources of uncertainty by probability density functions

5   inferred from observational data and expert assessment (characterisation of uncertainty), to deduce the impact of sources of uncertainty on projections (propagation of uncertainty) and to ascertain the impact of each source of uncertainty on the projection uncertainty and rank them in order of significance (stochastic sensitivity analysis). These developments have led to new theory and new methods that are of interest to be applied to uncertainty quantification of ice-sheet models, beyond the theory and methods that Golledge et al. (2015), Ritz et al. (2015), DeConto and Pollard (2016) and Schlegel et al. (2018) have

10   already applied.

In this paper, we apply probabilistic methods to assess the impact of uncertainties on the continental AIS response over the next millennium. We use the fast Elementary Thermomechanical Ice Sheet (f.ETISh) model (Pattyn, 2017), a hybrid ice-sheet model that captures the essential characteristics of ice flow and allows long-term and large-scale projections at a reasonable computational cost. To reduce the computational cost of assessing the impact of uncertainties on the change in global mean sea

15   level (GMSL), we draw from the UQ community methods based on the construction of an emulator, also known as a surrogate model, that is, a computational model that mimics the response of the original ice-sheet model at reduced computational cost. To assess the significance of each individual source of uncertainty in inducing uncertainty in the change in GMSL, we draw from the UQ community methods for stochastic sensitivity analysis. To express the uncertainty in projections of the retreat of grounded ice, we draw from the UQ community methods for constructing confidence regions for excursion sets.

20   On the one hand, our study adds to previous studies (Golledge et al., 2015; Ritz et al., 2015; DeConto and Pollard, 2016) that also provided projections for the multi-centennial response of the whole Antarctic ice sheet; yet, whereas these previous studies provided projections by running the ice-sheet model with samples of parameters from the parameter space, our study differs by the adoption of additional methods from the UQ community and the analysis of a broader set of parameters that includes uncertainty in climate forcing, basal sliding, grounding-line flux parameterisation, calving, sub-shelf melting, ice-shelf

25   rheology and bedrock relaxation. On the other hand, our study also adds to previous studies (Pollard et al., 2016; Schlegel et al., 2018) that also applied methods from UQ for uncertainty propagation in ice-sheet models; yet, whereas these previous studies analysed AIS paleoclimatic responses with Gaussian process (kriging) emulators (Pollard et al., 2016) and multi-decadal forecasts with Latin hypercube sampling (Schlegel et al., 2018), our study differs by its focus on the analysis of the multi-centennial response of the whole Antarctic ice sheet with polynomial emulators; and in addition to uncertainty propagation,

30   we complement our uncertainty analysis with stochastic sensitivity analysis and confidence regions.

This paper is organised as follows. First, Sect. 2 describes the f.ETISh model, the uncertain processes and parameters and the UQ methods, including the use of an emulator, stochastic sensitivity analysis and the construction of confidence regions. Subsequently, Sect. 3 shows and interprets the results for the multi-centennial response of the Antarctic ice sheet as well as the advantages of the adopted UQ methods. Finally, Sect. 4 provides an overall discussion of the results.

2 Model description and methods

2.1 Ice-sheet model and simulations

We use the fast Elementary Thermomechanical Ice Sheet (f.ETISh) model (Pattyn, 2017) version 1.2, a vertically integrated, thermomechanical, hybrid ice-sheet/ice-shelf model. The f.ETISh model incorporates essential characteristics of ice-sheet

5 thermomechanics and ice-stream flow, such as the mass-balance feedback, bedrock deformation, sub-shelf melting and calving. The ice flow is represented as a combination of the shallow-ice (SIA) and shallow-shelf (SSA) approximations for grounded ice (Bueler and Brown, 2009), while only the shallow-shelf approximation is applied for floating ice shelves. Grounding-line migration is represented at coarse resolution by a flux condition derived from a boundary layer theory at steady state either based on a Weertman (or power) friction law (Schoof, 2007) or a Coulomb friction law (Tsai et al., 2015) at the grounding line.

10 This flux condition at the grounding line is imposed as an internal boundary condition following the implementation by Pollard and DeConto (2009, 2012a), which was shown to reproduce grounding-line migration as predicted theoretically (Schoof, 2007; Pattyn et al., 2012, 2013). Bedrock deformation is represented as a combined time-lagged asthenospheric relaxation and elastic lithospheric response (Greve and Blatter, 2009; Pollard and DeConto, 2012a), in which the lithosphere relaxes towards isostatic equilibrium due to the viscous properties of the underlying asthenosphere. Calving at the ice front is parameterised based on the

15 large-scale stress field, represented by the horizontal divergence of the ice-shelf velocity field (Pollard and DeConto, 2012a).

The main changes in f.ETISh version 1.2 as compared to version 1.0 (Pattyn, 2017) consist of the implementation of an ocean model that approximates sub-shelf ocean circulation to determine sub-shelf melting, the inclusion of a laterally varying flexural rigidity for the lithosphere, a refinement of the positive degree-day model and an improvement of the SSA numerical scheme based on the implementation by Rommelaere and Ritz (1996).

20 We perform simulations of the response of the Antarctic ice sheet (Fig. 1a) to environmental and parametric perturbations over the period 2000–3000 CE. Input data include the present-day ice-sheet geometry and bedrock topography from the Bedmap2 dataset (Fretwell et al., 2013), the geothermal heat flux by An et al. (2015) and the spatially varying effective lithosphere thickness by Chen et al. (2017) to compute glacial isostatic adjustment more realistically with an elastic lithosphere/relaxed asthenosphere model. We perform simulations at a spatial resolution of 20 km, which allows to keep computa-

25 tional cost tractable. We found that the results with the f.ETISh model are essentially scale independent, as suggested by Pattyn (2017). The computational cost of a single forward simulation with a time step of 0.05 years on the CÉCI clusters (F.R.S-FNRS & Walloon Region) on 2 threads is approximately 8 h.

We drive our simulations with both atmospheric and oceanic forcings. Present-day mean surface air temperature and precipitation are obtained from Wessem et al. (2014), based on the regional atmospheric climate model RACMO2. Changes in

30 atmospheric temperature and precipitation rate induced by a forcing temperature change ΔT are applied in a parameterised way that accounts for elevation changes (Huybrechts et al., 1998; Pattyn, 2017). We use a positive degree-day (PDD) model to calculate surface melt (Janssens and Huybrechts, 2000), assuming a PDD factor of 3 mm$^\circ$C^{-1}day^{-1} and 8 mm$^\circ$C^{-1}day^{-1} for snow and ice, respectively. The PDD model also includes meltwater percolation and refreezing.

Basal melting underneath ice shelves is determined from the Postdam Ice-shelf Cavity mOdel (PICO) ocean-coupler model (Reese et al., 2018), which evaluates sub-shelf melting from the far-field ocean temperature and salinity fields via an ocean box model that captures the basic overtuning circulation within ice-shelf cavities. We employ data by Schmidtko et al. (2014) for present-day ocean temperature and salinity and apply a background oceanic temperature change over time linked to the

5   atmospheric forcing. Figure 1b shows the initial sub-shelf melt rate as computed with the PICO model. The PICO model is able to reproduce the general pattern of sub-shelf melting with higher melt rates near the grounding line and lower melt rates near the calving front. Sub-shelf melt rates are also higher in the Amundsen Sea sector and lower underneath the large Ross and Filchner–Ronne ice shelves.

The calibration of the basal sliding coefficient follows the data assimilation method of ice-sheet geometry by Pollard and

10   DeConto (2012b). This approach is based on a fixed-point iteration scheme that adjusts the basal sliding coefficient iteratively so as to match the present-day ice-sheet configuration while assuming that the present-day configuration is in steady state. After applying this approach, we further adjust the basal sliding coefficient in ice streams with a sliding multiplier factor similar to Bindschadler et al. (2013) to reduce the initial drift. We carry out the calibration step independently for the different sliding and grounding-line flux conditions investigated in this paper. For the nominal values of the model parameters and without

15   forcing anomaly, the initial drifts (reference runs) range from 0.1 to 0.2 metre of sea-level rise by 3000. To make our analysis insensitive to model initialisation, we correct all our results for this initial bias by subtracting the reference runs from the results. Therefore, after corrections for present-day dynamical changes, our results reflect the model response to perturbations.

2.2 Sources of uncertainty

We aim at quantifying the response of the Antarctic ice sheet to climate change while accounting for uncertainty in atmospheric

20   forcing, basal sliding, grounding-line flux parameterisation and physical model parameters relevant to ice-sheet dynamics (see Table 1). Here, we choose the uncertainty ranges for the parameters sufficiently large so as to encompass extreme conditions. The effect of choosing narrower uncertainty ranges for the parameters is discussed in Sect. 3.6. We assume the parameters to take the same value everywhere over the whole Antarctic ice sheet. This approach is likely to be conservative as the parameters may vary at least regionally. We refer to Schlegel et al. (2018) for a discussion about uncertainty quantification based on a

25   partitioning of the ice-sheet domain. In the remainder of this section, we list the uncertain parameters and briefly discuss their influence on the AIS response.

Table 1. Uncertain parameters.

Definition	Parameter	Nominal	Min	Max	Units
Sliding exponent	m	2	1	5	
Calving multiplier factor	F_{calv}	1	0.5	1.5	
Ocean melt factor	F_{melt}	0.3	0.1	0.8	
Shelf anisotropy factor	E_{shelf}	0.5	0.2	1	
East Antarctic bedrock relaxation time	τ_{e}	3000	2500	5000	yr
West Antarctic bedrock relaxation time	τ_{w}	3000	1000	3500	yr

2.2.1 Atmospheric forcing

Alongside oceanic forcing, atmospheric forcing is generally considered to be the primary driver for AIS dynamical changes. Simulating atmospheric forcing over several centuries with regional climate models is computationally prohibitive. In addition, the accuracy of the climate models is limited by uncertainties such as the possible trajectories of anthropogenic greenhouse gas emissions. Therefore, we adopt here the four schematic extended representative concentration pathway (RCP) scenarios RCP 2.6, RCP 4.5, RCP 6.0 and RCP 8.5 introduced by Golledge et al. (2015) for temperature changes in the atmosphere (Fig. 2) as a means of representing different atmospheric forcings relevant for policymakers.

The scenario plays a significant role in the amplitude and speed of the AIS retreat. Recent studies (Golledge et al., 2015; DeConto and Pollard, 2016) have shown no substantial retreat of the grounding-line position in the strongly mitigated RCP 2.6 scenario. The other scenarios lead to a reduction in the extent of the major ice shelves (Ross, Filchner–Ronne and Amery ice shelves) within 100–300 years, leading to accelerated grounding-line recession due to reduced buttressing. DeConto and Pollard (2016) have also highlighted that the hydrofacturing and ice cliff failure mechanisms (not included in the f.ETISh model version 1.2) driven by increased surface melt and sub-shelf melting could potentially lead to an accelerated collapse of the West Antarctic ice sheet and a deeper grounding-line retreat in the East Antarctic subglacial marine basins.

2.2.2 Basal sliding

Basal sliding controls the motion of fast-flowing ice streams, which drain about 90 % of the total Antarctic ice flux (Bennett, 2003). Several studies (Joughin et al., 2009, 2010; Ritz et al., 2015) have shown the importance of basal sliding on the behaviour of ice streams. In particular, Ritz et al. (2015) have shown that, under a power-law rheology for basal sliding, the contribution to future sea-level rise is an increasing function of the sliding exponent.

We introduce basal sliding as a Weertman sliding law, that is,

$$\boldsymbol{v}_b = -A_b \|\boldsymbol{\tau}_b\|^{m-1} \boldsymbol{\tau}_b, \tag{1}$$

where $\boldsymbol{\tau}_b$ is the basal shear stress, $\boldsymbol{v}_b$ the basal velocity, A_b the basal sliding coefficient and m a sliding exponent. We consider a nominal value of 2 for the last parameter as well as values of 1 and 3 to represent a viscous and a more plastic sliding

law, respectively. Hereafter, we refer to the exponents $m = 1, 2$ and 3 as the viscous (or linear), the weakly nonlinear and the strongly nonlinear sliding law, respectively. We consider the discrete values $m = 1, 2$ and 3 as representative of the most common values in large-scale ice-sheet modelling and discuss in Sect. 3.7 the impact of a more plastic sliding law ($m = 5$) to represent a quasi-plastic deformation of the till in ice streams (Gillet-Chaulet et al., 2016).

2.2.3 Grounding-line flux parameterisation

The f.ETISh model employs a parameterisation of the grounding-line flux based on a boundary layer theory at steady state by either Schoof (2007) (SGL) or Tsai et al. (2015) (TGL). For the TGL parameterisation, Pattyn (2017) has shown an increased AIS contribution to sea-level rise and a more significant retreat of the grounding line. We consider SGL parameterisation as the reference parameterisation for most of the simulations and discuss the impact of TGL parameterisation in Sect. 3.8.

We applied the TGL parameterisation under the weakly nonlinear sliding law. There is no consensus on the compatibility between the TGL parameterisation and the Weertman sliding law, as the TGL parameterisation was derived from the Coulomb friction law near the grounding line (Tsai et al., 2015). Yet, the Coulomb friction law is applicable in a narrow transition region in the vicinity of the grounding line not resolved on our coarse mesh, which lends validity to the combination of the TGL parameterisation and Weertman's sliding law.

2.2.4 Calving

Ice loss due to ice calving at the edges of ice shelves is responsible for almost half of the present-day ice mass loss of the Antarctic ice sheet (Depoorter et al., 2013; Rignot et al., 2013). Iceberg calving can have strong feedback effects as it affects ice-shelf buttressing and therefore ice flux at the grounding line and the stability of marine ice sheets (Schoof et al., 2017). It can also lead to a total disintegration of ice shelves followed by a potential marine ice cliff instability (Pollard et al., 2015).

We consider a multiplier factor F_{calv} in the parameterisation of the calving rate (Pollard and DeConto, 2012a; Pattyn, 2017). This approach is similar to Briggs et al. (2013) and Pollard et al. (2016). Here, we consider for F_{calv} a nominal value of 1.0 and an uncertainty range from 0.5 to 1.5, that is, the calving rate can vary between $50\ \%$ and $150\ \%$ of its nominal value.

2.2.5 Oceanic forcing

Sub-shelf melting is mainly controlled by sub-shelf ocean circulation, which can be affected by atmospheric changes. Ice-shelf thinning caused by increased sub-shelf melting leads to a reduction in ice-shelf buttressing. West Antarctica, where the bedrock lies mainly below sea level, is particularly vulnerable as suggested by observational (Rignot et al., 2014) and modelling (Favier et al., 2014; Joughin et al., 2014) studies.

We consider uncertainty in sub-shelf melting in a simple way by introducing an ocean melt factor F_{melt} that represents the ratio between oceanic and atmospheric temperature changes (Maris et al., 2014; Golledge et al., 2015). We consider for F_{melt} a nominal value of 0.3 (Maris et al., 2014; Golledge et al., 2015) and an uncertainty range from 0.1 to 0.8.

2.2.6 Ice-shelf rheology

Ice rheology in large-scale ice-sheet models is usually described as an isotropic material obeying Glen's flow law (Greve and Blatter, 2009). However, ice is known to be an anisotropic material whose fabric is dependent on the temperature field, the strain-rate history and the stress history (Ma et al., 2010; Calonne et al., 2017). For a given fabric, the anisotropic response
5   depends on the stress regime, which explains the ice stiffening when moving from a shear-dominated stress regime for grounded ice to an extension-dominated stress regime for floating ice.

We introduce a shelf tune parameter E_{shelf} that accounts for anisotropy between grounded and floating ice. A lower value makes ice shelves more viscous (Briggs et al., 2013; Maris et al., 2014). We consider for E_{shelf} a nominal value of 0.5 and an uncertainty range from 0.2 to 1, where a value of 0.5 means that the ice in the ice shelves is two times more viscous than
10   without shelf tuning.

2.2.7 Bedrock relaxation

Bedrock relaxation due to deglaciation may induce a negative feedback that promotes stability in marine portions and mitigates the effect of a marine ice-sheet instability (Gomez et al., 2010, 2013; Adhikari et al., 2014). The amplitude of the glacial isostatic uplift is determined by the flexural rigidity of the lithosphere and the viscous relaxation time of the asthenosphere.
15   Recent studies (van der Wal et al., 2015; Chen et al., 2017) have shown significant differences in the properties of the lithosphere and the asthenosphere between West and East Antarctica. van der Wal et al. (2015) have found a lower viscosity and therefore a lower relaxation time for Earth's mantle underneath West Antarctica, making the glacial isostatic uplift in this region more sensitive to changes in ice thickness.

We account for the differences between East and West Antarctica by introducing two characteristic relaxation times τ_{e} and
20   τ_{w} that we consider to both have a nominal value of 3000 years. We consider that τ_{e} has an uncertainty range from 2500 to 5000 years and τ_{e} has an uncertainty range from 1000 to 3500 years.

2.3 Uncertainty quantification methods

2.3.1 Characterisation of uncertainty

To quantify the impact of uncertainties on the AIS response, we adopt a probabilistic framework. Here, we assume, in the
25   absence of any prior information other than the aforementioned nominal values and minimal and maximal values of the uncertainty ranges, that the parameters F_{calv}, F_{melt}, E_{shelf}, τ_{e} and τ_{w} are uniform random variables with bounds given by the minimal and maximal values of their uncertainty ranges. We explore the uncertainty in the sliding exponent m by considering its nominal and extremal values separately, thus allowing to reduce the dimension of the parameter space while being consistent with other studies (Ritz et al., 2015). We limit the probabilistic characterisation to assuming uniform probability density
30   functions and we do not address how this probabilistic characterisation could be refined by using expert assessment, data and statistical methods such as Bayesian inference. Yet, we provide results that give some insight into the impact of the choice of

this probabilistic characterisation later in Sect. 3.6 and we refer the reader to Petra et al. (2014), Isaac et al. (2015), Ruckert et al. (2017), Gopalan et al. (2018) and Conrad et al. (2018) for applications of Bayesian inference in glaciology.

2.3.2 Propagation of uncertainty

Given the probabilistic characterisation of the uncertainty in the parameters, the propagation of uncertainty serves to assess

5   the impact of the uncertainty on the global mean sea-level change. In particular, its intent is to estimate the probability density functions for the change in GMSL as well as some of its statistical descriptors such as its mean, variance and quantiles. Various methods have been developed in the UQ community to estimate these statistical descriptors in a nonintrusive manner treating the ice-sheet model as a black box. Here, we use emulation methods based on a polynomial chaos (PC) expansion.

An emulator, also known as a surrogate model, is a computational model that mimics the ice-sheet model at low compu-

10   tational cost. Although emulators can also be obtained by Gaussian process regression (Rasmussen and Williams, 2006), we use polynomial chaos (PC) expansions (Ghanem and Spanos, 2003; Le Maître and Knio, 2010), which involve approximating the parameters-to-projection relationship as a polynomial in the parameters. We write this polynomial as a linear combination of polynomial basis functions and use least-squares regression (Appendix A) to evaluate the coefficients from a limited number of ice-sheet model runs at an ensemble of training points in the parameter space. The training points must be adequately

15   chosen in the parameter space (Hadigol and Doostan, 2018) and the convergence of the PC expansion must be assessed to ensure accuracy. PC expansion may suffer from limitations: PC expansion require the parameters-to-projection relationship to be sufficiently smooth (no discontinuity or highly nonlinear behaviour) to allow an efficient approximation as a low-degree polynomial and PC expansions may be inefficient in high-dimensional problems.

The emulator of the relationship between the parameters and the projection is then used as a substitute for the ice-sheet

20   model in a Monte-Carlo method (Robert and Casella, 2013), in which samples of the parameters are drawn randomly from their probability density function and mapped through the emulator into corresponding samples of the projections. Approximations to the probability density function of the projection and its statistical descriptors are then obtained from these samples of the projections by using statistical estimation methods: for instance, the mean and quantiles are approximated with the sample mean and quantiles.

25   The use of an emulator has the following advantages: (i) it provides an inexpensive approximation of the ice-sheet model that accelerates UQ analysis; (ii) it provides an explicit view on the relationship between the parameters and the projection, highlighting potential linear or nonlinear dependences and interactions between the parameters; (iii) it allows to interpolate efficiently the projections in the parameter space; (iv) it can be used to carry out stochastic sensitivity analysis to assess the influence of each parameter on the projections; (v) under certain conditions, the same emulator can be reused between UQ

30   analyses with different probability density functions for the parameters and (vi) it can be used for Bayesian calibration (Ruckert et al., 2017).

We built a separate PC expansion for each combination of RCP scenario, sliding law and grounding-line flux parameterisation. For each combination, we generated an ensemble of 500 forward simulations; for each time instant of analysis, we fitted to this ensemble a polynomial chaos expansion of degree 3, which we then used as emulator to evaluate the statistical

descriptors, except the confidence regions, which we deduced directly from the forward simulations. We present a convergence study and cross-validation in Appendix A.

2.3.3 Stochastic sensitivity analysis

Stochastic sensitivity analysis serves to identify which uncertain parameters and their associated physical phenomenon are most influential in inducing uncertainty in the ice-sheet response. Here, we adopt the variance-based sensitivity indices (Saltelli et al., 2008), also called Sobol indices, described in more detail in Appendix B. Variance-based sensitivity indices rely on the decomposition of the variance of the projections as a sum of contributions from each uncertain parameter taken individually and an interaction term. Then, the Sobol index of a given uncertain parameter represents the fraction of the variance of the projections explained as stemming from this sole uncertain parameter. A Sobol index takes values between 0 and 1, whereby a value of 1 indicates that the entire variance of the projections is explained by this sole uncertain parameter, and a value of 0 indicates that the uncertain parameter has no impact on the projection uncertainty.

We compute the Sobol indices directly from the PC coefficients (Crestaux et al., 2009; Le Gratiet et al., 2017).

2.3.4 Confidence regions for grounded-ice retreat

To gain insight into the impact of the uncertainty in determining which subregions of Antarctica are most at risk of ungrounding, we construct confidence regions for grounded ice for several probability levels. We define a confidence region for grounded ice for a given probability level as a subregion of Antarctica that remains covered everywhere with grounded ice with a probability of at least the given probability level under the uncertainty introduced in the ice-sheet model (see Appendix C for the mathematical definition). The differences between these confidence regions for grounded ice for different probability levels provide insight into the risk of ungrounding (see Sect. 3.5). Such confidence regions are useful because confidence regions with boundaries far from the initial grounding line may indicate an important MISI and large differences between confidence regions for different probability levels indicate significant impact of the uncertainty on the ice-sheet ungrounding. We construct these confidence regions for grounded ice based on an extension of previous work by Bolin and Lindgren (2015) for Gaussian random fields to our glaciological context.

3 Results

We present nominal and probabilistic projections (relative to 2000 CE) for short-term (2100), medium-term (2300) and long-term (3000) time scales under different RCP scenarios and sliding laws. All results to follow have been obtained with the SGL parameterisation for the grounding-line migration, except in a discussion at the end of the section, where we discuss the impact of using the TGL parameterisation.

3.1 Nominal projections

We first present nominal projections obtained using the nominal values of the parameters given in Table 1 We first present results under nominal conditions in order to assess subsequently the impact of uncertainties on AIS sea-level rise projections. Under nominal conditions, we find (Table 2) in RCP 2.6 a nominal AIS contribution to sea-level rise of 0.02 m by 2100, 0.07 m

5 by 2300 and 0.20 m by 3000 and in RCP 8.5 a nominal AIS contribution to sea-level rise of 0.05 m by 2100, 0.59 m by 2300 and 3.9 m by 3000. In Fig. 3a, we represented the nominal projections as a function of time in all RCP scenarios. We find that the nominal AIS contribution to sea-level rise is rather small in the first decades and starts to increase more significantly around 2100 with a rather constant growth rate. In Fig. 3b–e, we represented the nominal grounded ice region by 3000 for all RCP scenarios. We find that there is little ungrounding by 3000 in RCP 2.6 and RCP 4.5, while we observe a more significant

10 ungrounding in Siple Coast and the Ronne basin in RCP 6.0 and a much more significant ungrounding in Siple Coast and the Amundsen Sea sector in RCP 8.5.

Year	RCP 2.6	RCP 4.5	RCP 6.0	RCP 8.5
2100	0.02	0.01	0.03	0.05
2300	0.07	0.10	0.22	0.59
3000	0.20	0.39	0.86	3.90

Table 2. Nominal projections (in metres) of AIS contribution to sea-level rise on short-term (2100), medium-term (2300) and long-term (3000) time scales in different RCP scenarios.

3.2 Parameters-to-projections relationship

One of the advantages of a polynomial chaos expansion is that it provides an explicit approximation to the parameters-to-projections relationship, which can be visualised to gain insight into the relationship between the parameters and the projec-

15 tions.

In Fig. 4 and 5, we used the PC expansions to visualise how the projections depend on each parameter individually (one-at-a-time) while keeping the other parameters fixed at their nominal value under the weakly nonlinear sliding law in RCP 2.6 and RCP 8.5, respectively.

Figure 4a–c shows that in RCP 2.6 ΔGMSL increases with an increase in the calving factor nonlinearly . The slope is steeper

20 for small values of this parameter, thus suggesting that ΔGMSL is more sensitive to small changes about small values than about higher values. Figures 4d–f indicate that ΔGMSL increases rather linearly with an increase in the melt factor. Fig. 4g–i indicate a rather quadratic dependence on the shelf anisotropy factor for short-term and medium-term projections, with small and large values of this factor leading to more significant ice loss than the nominal value. This rather quadratic dependence can be explained by the influence of E_{shelf} on two competing processes: on the one hand, a higher value of E_{shelf} softens the

25 ice, thus leading to faster ice flow in the ice shelves; on the other hand, a higher value of E_{shelf} leads to ice-shelf thinning, thus making ice flux at the grounding line less important. In addition, we find that ΔGMSL depends only little on the bedrock

relaxation times (Fig. 4j–o). In fact, lower bedrock relaxation times do tend to stabilise the ice sheet and lower sea-level rise but this impact is weak compared to the influence of the other parameters. This result may be explained by our orders of magnitude of the bedrock relaxation times being of the order of a few millennia, thus preventing any significant uplift in the next few centuries. Yet, recent studies (Barletta et al., 2018) have suggested a bedrock relaxation time scale of the order of decades to

5   a century in the Amundsen Sea sector, thus making glacial isostatic adjustment significant in the next decades and centuries in this region. To assess the influence of shorter relaxation times, we performed additional numerical experiments, albeit not reported in this paper, with a relaxation time for the whole West Antarctic ice sheet that varies widely from a few decades to a few millennia. For this range of values, we found that bedrock relaxation has a more significant influence on the AIS response.

We find in RCP 8.5 similar trends. However, whereas F_{calv}, F_{melt} and E_{shelf} influence ΔGMSL equally significantly in

10   RCP 2.6, the melt factor influences ΔGMSL most significantly in RCP 8.5. Whereas Fig. 5d–e shows that ΔGMSL increases rather linearly with an increase in the melt factor, Fig. 5f shows that ΔGMSL rather levels off at a plateau for large values of sub-shelf melting for long-term projections in RCP 8.5.

Additionally, Fig. S1 shows the emulators for several pairs of parameters with the other parameters fixed at their nominal values in RCP 2.6 and RCP 8.5. These figures show essentially the same trends as those identified in Fig 4 and 5, in addition to

15   interaction effects between the parameters. In particular, we find that smaller calving and sub-shelf melting lead to mass gain (Fig. S1c), while large values of the shelf anisotropy and melt factors lead to important mass loss (Fig. S1d).

3.3   Sea-level rise projections

Under parametric uncertainties, we find (Table 3, Fig 6) in RCP 2.6 a median AIS contribution to sea-level rise of 0.02–0.03 m by 2100, 0.07–0.13 m by 2300 and 0.18–0.30 m by 3000, as compared with the nominal projection of 0.02 m by 2100, 0.07 m

20   by 2300 and 0.20 m by 3000; and we find in RCP 8.5 a median AIS contribution to sea-level rise of 0.09–0.11 m by 2100, 0.78–1.15 m by 2300 and 3.18–6.12 m by 2500, as compared with the nominal projection of 0.05 m by 2100, 0.59 m by 2300 and 3.59 m by 3000. The median AIS sea-level rise projections are higher than the nominal projections, except for a certain cases under the viscous sliding law. The nominal projections are not equal to the median projections because the ice-sheet model exhibits nonlinearities, as illustrated in Fig. 4 and 5, and the probability density functions for the parameters are not

25   symmetric about their nominal value. As in the nominal projections, we find that in all RCP scenarios and under all sliding laws, the median AIS contribution to sea-level rise is rather small in the first decades and starts to increase more significantly around 2100. As in the nominal projections, the median AIS contribution to sea-level rise shows a rather constant growth rate in RCP 2.6, RCP 4.5 and RCP 6.0; contrary to the nominal projection, the median AIS contribution to sea-level rise exhibits initially an acceleration before subsequently exhibiting a deceleration in RCP 8.5 under both nonlinear sliding laws. This

30   behaviour in the median projections in RCP 8.5 is a consequence of the initial rapid collapse of the West Antarctic ice sheet, which contributes to sea-level rise by 3–3.5 metres, followed by a slower retreat in the East Antarctic ice sheet. By contrast, the nominal projections, which involve a melt factor of 0.3, indicate that the West Antarctic ice sheet does not completely collapse by 3000.

We find (Table 3) in RCP 2.6 5–95 % probability intervals for sea-level rise projections that range from -0.06 to 0.10 m by 2100, from -0.14 to 0.31 m by 2300 and from -0.36 to 0.91 m by 3000 in RCP 8.5 and from -0.03 to 0.23 m by 2100, 0.17 to 2.01 m by 2300 and 0.82 to 7.68 m by 3000. The nominal projections are inside the 5 %–95 % probability intervals. We see that the 5–95 % probability intervals indicate an increase in sea-level rise even if a decrease in sea-level rise cannot

5   be ruled out especially under the viscous sliding law and cooler atmospheric conditions, with, for instance, a probability of about 6 % of negative sea-level rise by 3000 in RCP 2.6 under the weakly nonlinear sliding law. Figure 6 highlights that the 33 %–66 % probability intervals become wider under warmer atmospheric conditions and, to a lesser extent, more nonlinear sliding conditions. The uncertainty in the projections due to parametric uncertainty is rather significant, with possible overlaps between the 5 %–95 % probability intervals for different RCP scenarios. For instance, Fig. 4i shows that a contribution to

10   sea-level rise of about 0.7 m can be reached by 3000 in RCP 2.6 for the extreme value $E_{\mathrm{shelf}} = 1$, while Fig. 5f shows that this value is reached in RCP 8.5 for very limited sub-shelf melting (F_{melt} of about 0.12). This suggests that projections with similar contributions to sea-level rise can arise in different RCP scenarios with different combinations of parameter values. Measuring the relative dispersion in ΔGMSL via the coefficients of variation, that is, the ratio between the standard deviation and the mean value, we find a coefficient of variation of 0.74 in RCP 2.6, 0.67 in RCP 4.5, 0.59 in RCP 6.0 and 0.33 in RCP

15   8.5 by 3000 under the weakly nonlinear sliding law. This demonstrates that the relative uncertainty in ΔGSLM projections is higher in cooler RCP scenarios.

Figure 7 shows the probability density functions for the change in GMSL at different time scales. The results display essentially unimodal probability density functions with wider tails for warmer scenarios and longer time scales. In RCP 2.6, the probability density functions resemble Gaussian probability density functions. In RCP 8.5 and at the short and medium

20   time scales, the probability density functions are rather flat, which can be explained by the dependence of ΔGMSL on it being rather linear (Fig. 5d and e). In RCP 8.5 and at the long time scale, the probability density functions exhibit a more localised mode at higher values of ΔGMSL, which can be explained by the collapse of the West Antarctic ice sheet and thus the presence of the plateau for higher values of the melt factor (Fig. 5f).

Figure 8 gives the probability of exceeding the threshold values of 0.5 m, 1.0 m and 1.5 m as a function of time. We find

25   that the probability of exceeding 0.5 m by 2100 is negligible (probability of less than 1 %) in all RCP scenarios and under all sliding conditions in RCP 2.6, the AIS contribution to sea-level rise in the next centuries is strongly limited, with a probability of exceeding 0.5 m by 3000 reaching at most 30 %. In RCP 4.5 and RCP 6.0, we found nominal sea-level rise projections well below 1.5 m, while in RCP 8.5 this threshold is exceeded. In the presence of uncertainties, we find that the probability of exceeding 1.5 m of sea-level rise by 3000 can reach about 35 % in RCP 4.5, about 70 % in RCP 6.0 and about 95 % in RCP 8.5.

30   The last result can be seen from Fig. 5, which indicates that ΔGMSL is below 1.5 m only in a small region of the parameter space associated with small values of the melt factor. Furthermore, the shape of the exceedance curves in Fig. 8 provides some insight into the uncertainty in the time when a certain threshold value is exceeded. The time when ΔGMSL exceeds 0.5 m with a probability of 33 % under the weakly nonlinear sliding law is 2415 in RCP 4.5, 2270 in RCP 6.0 and 2185 in RCP 8.5 while this value is exceeded with a probability of 66 % at 2790 in RCP 4.5, 2430 in RCP 6.0 and 2245 in RCP 8.5. We find

that nominal projections overestimate the time when ΔGMSL exceeds 0.5 m, with the exceedance time being beyond 3000 in
RCP 4.5, around 2620 in RCP 6.0 and around 2280 in RCP 8.5.

Year	Sliding (m)	RCP 2.6	RCP 4.5	RCP 6.0	RCP 8.5
2100	1	0.02 (-0.06–0.10)	0.04 (-0.05–0.12)	0.05 (-0.04–0.13)	0.09 (-0.03–0.20)
	2	0.03 (-0.01–0.09)	0.05 (0.00–0.11)	0.06 (0.00–0.14)	0.11 (0.01–0.22)
	3	0.03 (-0.03–0.09)	0.04 (-0.02–0.11)	0.06 (-0.01–0.14)	0.11 (0.00–0.23)
2300	1	0.07 (-0.14–0.31)	0.20 (-0.09–0.48)	0.36 (-0.04–0.72)	0.78 (0.17–1.35)
	2	0.13 (0.01–0.30)	0.26 (0.03–0.54)	0.45 (0.06–0.88)	1.04 (0.27–1.81)
	3	0.09 (-0.09–0.29)	0.28 (-0.03–0.58)	0.50 (0.02–0.96)	1.15 (0.31–2.01)
3000	1	0.18 (-0.36–0.82)	0.77 (-0.14–1.82)	1.60 (-0.01–2.71)	3.18 (0.82–4.25)
	2	0.30 (-0.01–0.82)	0.93 (0.08–2.24)	2.16 (0.15–4.06)	5.08 (1.36–6.00)
	3	0.30 (-0.25–0.91)	1.15 (0.08–2.56)	2.50 (0.34–5.17)	6.12 (1.65-7.68)

Table 3. Probabilistic projections (in metres) of the AIS contribution to sea-level rise on short-term (2100), medium-term (2300) and long-term (3000) time scales in different RCP scenarios and under different sliding conditions with Schoof's grounding-line parameterisation. ΔGMSL projections are the median projections with their 5–95 % probability intervals between parentheses.

3.4 Stochastic sensitivity analysis

Figure 9 provides the Sobol sensitivity indices for the change in GMSL on short-term, medium-term and long-term time scales
in different RCP scenarios and under different sliding laws. We find that in RCP 2.6, the largest contribution to the uncertainty
in ΔGMSL stems from the uncertainty in the ice-shelf rheology (Sobol indices ranging from 40 % to 60 %) followed by the
uncertainty in the calving rate (Sobol indices ranging from 20 % to 40 %) and sub-shelf melting (Sobol indices ranging from
5 % to 25 %). Indeed, in RCP 2.6, sub-shelf melting plays only a limited role because ocean conditions remain essentially
unchanged. Therefore, in RCP 2.6, the dispersion in ΔGMSL is mainly controlled by the ice-shelf rheology, which controls
ice-flow and buttressing in ice shelves, as well as calving, which reduces the extent of ice shelves and their buttressing.

By contrast, in warmer RCP scenarios and for longer time scales, the dominant source of uncertainty becomes the uncertainty
in sub-shelf melting, which accounts in RCP 8.5 for more than 90 % of the uncertainty in the sea-level rise projections. As
shown in Fig. 5, in RCP 8.5 at 3000 ΔGMSL varies by several meters over the range of values of F_{melt}, while ΔGMSL varies
only by a few tenths of centimetres over the range of values of the other parameters. Hence, the dominant influence of the
uncertainty in the melting factor is also a consequence of the rather wide uncertainty range that we chose for this parameter.

Finally, we find that, in all RCP scenarios and under all sliding laws, the uncertainty in the bedrock relaxation times for
West and East Antarctica has a limited impact (Sobol index smaller than 1 %), which is a direct consequence of the very

limited dependence of the projections on the bedrock relaxation times. Moreover, the interactions between the parameters have a negligible impact as the sums of the individual Sobol indices account almost entirely for the variances of the projections.

3.5 Projections of grounded-ice retreat

Figure 10 provides insight into the subregions of Antarctica that are most at risk of ungrounding in different RCP scenarios
5 and at different time scales under the weakly nonlinear sliding law. Figure 10 was obtained as follows. First, we determined the 100 % confidence region for grounded ice, that is, the subregion of Antarctica where ice is certain to remain grounded and we coloured it in grey. Thus, there is no risk that the grounding line retreats to within the grey region. Then, we determined the 95 % confidence region for grounded ice, that is, the subregion of Antarctica that remains covered everywhere with grounded ice with a probability of more than 95 %, and we coloured the portion of the 95 % confidence region that extends beyond the
10 100 % confidence region in dark blue. Thus, there is a low risk of (less than) 5% that the grounding line retreats to within the dark blue region. We continued this procedure for decreasing values of the confidence level and using different colours as indicated in the legend in Fig. 10.

We find that ice is certain to remain grounded in regions above sea level. By contrast, in all RCP scenarios, the risk of ungrounding is highest in marine sectors of West Antarctica with fast flowing ice streams, especially in Siple Coast, in the
15 Ronne basin notably the Ellsworth land and in the Amundsen Sea sector. In warm RCP scenarios and at longer time scales, we also observe a risk of grounding-line retreat in the Wilkes marine basin in East Antarctica, where the grounding line could retreat between 100 km (with a risk of 95 %) and 500 km (with a risk of 5 %) from its present-day position. The risk of retreat in Wilkes basin may partially explain the acceleration in sea-level rise that we observed in Fig. 6 in RCP 8.5. The risk of grounding-line retreat in the Antarctic Peninsula is very limited due to the bedrock topography being above sea level, the
20 marine glaciers being small and a high increase in precipitation in this region.

In RCP 2.6, we observe that the grounding line is quite stable over the next millennium, with the 100 % confidence region for grounded ice being almost unchanged from the present-day grounded ice region (differences between both regions are only of few tenths of kilometres by 3000). In RCP 4.5, ice is certain to remain grounded in most of the West Antarctic ice sheet over the next centuries, but our results also suggest a risk of retreat of the grounding line in some sectors of West Antarctica
25 on longer time scales. In RCP 6.0, we find that the West Antarctic ice sheet belongs by 3000 to the 66 % confidence region for grounded ice, while in RCP 8.5, it belongs by 3000 only to the 5 % confidence region. This suggests a risk of 33 % that a major collapse of the West Antarctic ice sheet might occur in RCP 6.0 by 3000 and a risk of 95 % that a major collapse of the West Antarctic ice sheet might occur in RCP 8.5 by 3000.

As compared with the nominal projections of a limited retreat of the grounding line in West Antarctica in RCP 6.0 by 3000,
30 we find that the impact of the parametric uncertainty is that a complete collapse of the West Antarctic ice sheet may occur with a risk of 33 % in RCP 6.0 by 3000. Moreover, Fig. 3e suggests that a complete disintegration of the West Antarctica ice sheet is underway by 3000 in RCP 8.5, while in Fig. 10l the West Antarctica has already collapsed by 3000.

Additionally, we compared the projections under the weakly nonlinear sliding law with projections under the other sliding laws, that is the viscous sliding law (Fig. S6) and the strongly nonlinear sliding law (Fig. S7). We find a lower risk of retreat of

the grounding line under the viscous sliding law with a slower disintegration of the West Antarctic ice sheet compared to the other sliding laws, especially in the drainage basins of Thwaites and Pine Island glaciers, which belong to the 50 % confidence region for grounded ice by 3000 in RCP 8.5, while they belong to the 5 % confidence region by 3000 in RCP 8.5 for the other sliding laws. The strongly nonlinear sliding law seems to favour a faster and deeper retreat of the grounding line especially

5   in the marine sectors of East Antarctica and the drainage basins of Thwaites and Pine Island glaciers. However, Fig. 10i and Fig. S7i suggest that ungrounding may be less significant in Siple Coast under the strongly nonlinear sliding law than the weakly nonlinear sliding law. Actually, MISI may occur when driving stresses overcome resistive stresses (Waibel et al., 2018). Driving stresses are primarily determined by the surface slopes, while resistive stresses depend on the basal sliding coefficient and the ice velocity through the sliding exponent. Driving stresses at the grounding line are higher in the Amundsen Sea sector

10   than in Siple Coast due to steeper surface slopes, leading to a greater sensitivity of the grounding line in the former region to nonlinearity and a more viscous response.

3.6 Influence of the parameter probability density function

We now address the influence of the probabilistic characterisation of the parametric uncertainty on our probabilistic projections. We represent the uncertain parameters F_calv, F_melt, E_shelf, τ_e and τ_w by a family of uniform probability density functions in-

15   dexed by a unique scaling factor α that controls the supports of the uniform probability density functions. For F_calv, the support is $[F_\mathrm{calv,nom} + \alpha(F_\mathrm{calv,min} - F_\mathrm{calv,nom}), F_\mathrm{calv,nom} + \alpha(F_\mathrm{calv,max} - F_\mathrm{calv,nom})]$, where $F_\mathrm{calv,nom}$, $F_\mathrm{calv,min}$ and $F_\mathrm{calv,max}$ are the nominal, minimum and maximum values in Table 1. For the other parameters, the supports are defined similarly. The value $\alpha = 0$ represents the ice-sheet model without parametric uncertainty, that is, the ice-sheet model for the nominal values of the parameters, and the value $\alpha = 1$ represents the full uncertainty ranges considered so far. We propagated the uncertainty from

20   the parameters to the sea-level rise projections for different values of the scaling factor reusing the emulator that we had built for $\alpha = 1$ over the whole parameter space. Hence, the projections to follow for $\alpha = 0$ based on this emulator are not exactly equal to the nominal projections determined directly from the ice-sheet model.

For the long-term projections, Fig. 11a–d show the median and the 33–66 % and 5–95 % probability intervals as a function of the scaling factor in the different RCP scenarios under the weakly nonlinear sliding law and Fig. 11e–h show the probability

25   density functions for the values $\alpha = 0.2, 0.4$ and 1.0. We find that the median projections increase with an increase in the scaling factor and range in RCP 2.6 from 0.15 m to 0.29 m, in RCP 4.5 from 0.40 m to 0.93 m, in RCP 6.0 from 1.13 m to 2.12 m and in RCP 8.5 from 3.83 m to 5.07 m. In addition, the width of the probability intervals increases with increasing uncertainty in the parameters. While the width of the 33–66 % probability interval increases rather linearly with the scaling factor and is rather symmetric about the median, the width of the 5–95 % probability interval increases more nonlinearly with

30   an increase in the scaling factor, as illustrated in Fig. 11a in RCP 2.6 and Fig. 11d in RCP 8.5. The probability density functions attribute higher weight to larger values of ΔGMSL under increased parametric uncertainty and increased weight given to larger values of in particular E_shelf in RCP 2.6 (Fig. 4i) and F_melt in RCP 8.5 (Fig. 5f). Figure 11a–d shows that the sensitivity of the amount of uncertainty in the projections (probability intervals) to the amount of uncertainty in the parameters (scaling factor)

is higher for warmer scenarios (with an upper bound between RCP 6.0 and RCP 8.5 as a consequence of the collapse of the West Antarctic ice sheet).

3.7 Projections under a more plastic sliding law

We ran the same ensemble of simulations under a more plastic sliding law ($m = 5$). Table 4 and Fig. 12 give for the AIS contribution to sea-level rise the median and the 33–66 % and 5–95 % probability intervals. We find in RCP 2.6 a median AIS contribution to sea-level rise of 0.03 m by 2100, 0.14 m by 2300 and 0.37 m by 3000 and we find in RCP 8.5 a median AIS contribution to sea-level rise of 0.13 m by 2100, 1.24 m by 2300 and 5.74 m by 3000. The 5–95 % probability intervals range in RCP 2.6 from -0.02 m to 0.08 m by 2100, from -0.02 m to 0.32 m by 2300 and from -0.07 m to 0.92 m by 3000. In RCP 8.5, the 5–95 % probability intervals range from 0.01 m to 0.25 m by 2100, from 0.40 m to 2.19 m by 2300 and from 1.92 m to 7.03 m by 3000. As compared with less plastic sliding laws, we find an increase in sea-level rise projections on short-term and medium-term time scales, thus suggesting a more significant and faster response to perturbations under more plastic sliding conditions. On a long-term time scale, the ice-sheet mass loss can be less important under $m = 5$ than $m = 3$, as observed in the median projections by 3000 in RCP 4.5 and RCP 8.5.

We find that overall the AIS contribution to sea-level rise is an increasing function of the sliding exponent, with the differences between successive exponents getting smaller as m increases, as already pointed out by Gillet-Chaulet et al. (2016); for instance, we observe a greater difference in the projections between $m = 1$ and $m = 2$ than between $m = 3$ and $m = 5$. On longer time scales, tipping points and nonlinearities associated with MISI may trigger a slightly different response of the ice sheet depending on the initial conditions, which could explain the smaller ice loss in our results under $m = 5$ than $m = 3$.

Year	RCP 2.6	RCP 4.5	RCP 6.0	RCP 8.5
2100	0.03 (-0.02–0.08)	0.05 (-0.01–0.12)	0.07 (-0.01–0.15)	0.13 (0.01–0.25)
2300	0.14 (-0.02–0.32)	0.34 (0.04–0.61)	0.56 (0.10–0.99)	1.24 (0.40–2.19)
3000	0.37 (-0.07–0.92)	1.07 (0.17–2.56)	2.70 (0.41–5.16)	5.74 (1.92–7.03)

Table 4. Same as Table 3 but with sliding exponent $m = 5$.

3.8 TGL parameterisation

We ran the same ensemble of simulations under the weakly nonlinear sliding law using, this time, the TGL parameterisation instead of the SGL parameterisation. Under the TGL parameterisation, Table 5 and Fig. 13 give for the AIS contribution to sea-level rise the median and the 33–66 % and 5–95 % probability intervals. We find an overall increase in sea-level projections compared to our results under Schoof's parameterisation. This result was expected as the TGL parameterisation has been shown to increase grounding-line sensitivity to environmental changes (Tsai et al., 2015; Pattyn, 2017). The 5–95 % probability intervals range in RCP 2.6 from 0 m to 0.14 m by 2100, from 0.02 m to 0.47 m by 2300 and from 0 m to 1.30 m by 3000. In RCP 8.5, the 5–95 % probability intervals range from 0.05 m to 0.37 m by 2100, from 0.59 m to 3.12 m by 2300 and from

3.85 m to 10.79 m by 3000. We find that the probability of exceeding 0.5 m by 2100 is still negligible (probability of less than 1 %) in all RCP scenarios. However, the probability of exceeding 0.5 m and 1 m by 3000 in RCP 2.6 can reach more than 40 % and 10 %, respectively. For other scenarios, the retreat of the Antarctic ice sheet is much more pronounced and faster than under the SGL parameterisation and the probability to exceed 1.5 m of sea-level rise by 3000 can reach more than 50 %

5 in RCP 4.5, 80 % in RCP 6.0 and 99 % in RCP 8.5.

Figures 10m–o show the confidence regions for grounded ice under the TGL parameterisation and RCP 8.5. As also pointed out by Pattyn (2017), the TGL parameterisation leads to a faster and more significant grounding-line retreat in the marine sectors and an additional mass loss from East Antarctica, especially in the Aurora basin.

Year	RCP 2.6	RCP 4.5	RCP 6.0	RCP 8.5
2100	0.06 (0.00–0.14)	0.10 (0.02–0.19)	0.12 (0.02–0.23)	0.21 (0.05–0.37)
2300	0.20 (0.02–0.47)	0.47 (0.10–0.89)	0.83 (0.18–1.43)	1.85 (0.59–3.12)
3000	0.46 (0.00–1.30)	1.73 (0.22–2.91)	3.47 (0.76–5.37)	7.43 (3.85–10.79)

Table 5. Same as Table 3 but with the TGL parameterisation.

4 Discussion

10 ### 4.1 Comparison of the sea-level rise projections with previous work

Regarding the short-term AIS contribution to sea-level rise, we projected in the RCP 2.6 scenario a median of 0.02–0.03 m under the SGL parameterisation and 5–95 % probability intervals from -0.07 m to 0.10 m. These projections are similar to other estimates based on other mechanisms. Golledge et al. (2015) reported an AIS contribution to sea-level rise between -0.01 m and 0.10 m with the lower and higher bounds corresponding to the absence and presence of sub-grid interpolation of basal melting at the grounding line. DeConto and Pollard (2016) reported an AIS contribution to sea-level rise between -0.11 m

15 and 0.15 m based on a model calibration with a range of Pliocene sea-level targets between 5 and 15 m higher than today. In the same scenario, we found an increased AIS response under the TGL parameterisation with a median AIS contribution to sea-level rise of 0.06 m and a 5–95 % probability interval between 0.01 m and 0.14 m by 2100. These higher projections are similar to the higher projections (0–0.22 m) reported by DeConto and Pollard (2016) for a higher range of Pliocene sea-level

20 targets between 10 and 20 m. In all RCP scenarios, under all sliding laws and under both grounding-line parameterisations, our results suggested that the AIS contribution to sea-level rise does not exceed 0.5 m by 2100 with a probability of at least 99 %. These results are in agreement with Ritz et al. (2015), who determined an AIS contribution to sea-level rise that lies between 0.05 m and 0.30 m, and Golledge et al. (2015), who found an AIS contribution to sea-level rise that reaches at most 0.38 m in RCP 8.5 with sub-grid interpolation of basal melting at the grounding line. Yet, projections by DeConto and Pollard (2016)

25 and Schlegel et al. (2018), who applied the more sensitive Budd-type friction law (Brondex et al., 2017), can exceed 0.5 m and even 1 m, but these higher projections are under extreme and maybe unrealistic warming conditions.

Regarding the long-term AIS contribution to sea-level rise, our projections under the SGL parameterisation are similar to other estimates by Golledge et al. (2015). In particular, both studies suggest that the AIS contribution to sea-level rise by 3000 in RCP 2.6 is limited to less than 1 m with a probability estimated to be at least 95 % in our study, while an AIS contribution to sea-level rise above 1.5 m by 3000 may arise in all other RCP scenarios. Yet, our long-term projections are generally below

5 projections by DeConto and Pollard (2016) with hydrofracturing and ice cliff failure mechanisms especially under warmer RCP scenarios, but the discrepancies between the projections of both models are reduced under the TGL parameterisation. In RCP 2.6, our projections by 2500 under the TGL parameterisation range from 0.04 m to 0.73 m, which is similar to projections by DeConto and Pollard (2016), which range respectively from -0.23 m to 0.61 m and 0.02 m to 0.48 m for the lower and higher range of Pliocene of sea-level targets.

10 ## 4.2 Comparison of the impact of parametric uncertainty with previous work

Similarly to Golledge et al. (2015, 2017), our study emphasised the pivotal role played by atmospheric forcing and sub-shelf melting as critical drivers of ice-sheet dynamics through ice-shelf thinning and subsequent reduced buttressing. As in Ritz et al. (2015), we found that the AIS contribution to sea-level rise is an increasing function of the sliding exponent, thus meaning that more plastic sliding conditions speed up the ice flow and consequently ice loss. Following Pattyn (2017), we highlighted

15 the greater sensitivity of the grounding-line migration under the TGL parameterisation, pointing out the key role played by physical processes in the vicinity of the grounding line.

4.3 Comparison of projections of grounded-ice retreat with previous work

Consistent with our results, Golledge et al. (2015), with a 10-km resolution model, projected that grounding-line retreat is most significant in the Siple Coast region. However, Ritz et al. (2015), based on the probability of MISI onset, as well as Cornford

20 et al. (2015), with a sub-kilometre resolution around the grounding line, projected that grounding-line retreat is most significant in the Amundsen Sea sector. Schlegel et al. (2018) found that grounding-line retreat is most significant in the Amundsen Sea sector, but, after tuning certain parameters region by region, they found that the western Ronne basin has the greater sensitivity. These discrepancies between our findings and those of Cornford et al. (2015), Ritz et al. (2015) and Schlegel et al. (2018) may be explained by our ocean model which may overestimate sub-shelf melting underneath Ross ice shelf and underestimate ocean

25 circulation in the Amundsen Sea and by our initialisation method which may underestimate the basal sliding coefficients for Thwaites and Pine Island glaciers. Moreover, the lower sensitivity of the Amundsen Sea sector may arise in our findings from shortcomings in the buttressing parameterisation, our low resolution not capturing properly the bedrock topography, the small pinning points and the flow dynamics in the narrower sectors of the ice sheet and our representation of calving, which may increase the instability threshold; see, for instance, Arthern and Williams (2017) and Waibel et al. (2018) for more thorough

30 discussions about the instability threshold in the Amundsen Sea sector.

4.4 Projections of ice loss and grounding-line retreat under parametric uncertainty

The significance of the contribution of the Antarctic ice sheet to sea-level rise under climate change is primarily controlled by the contribution of marine drainage basins, with the West Antarctic ice sheet more vulnerable than the East Antarctic ice sheet. The instability of marine drainage basins and their ability to trigger accelerated ice loss and significant grounding-line

5 retreat is determined by bedrock topography and ice-shelf buttressing which depends on the importance of ice-shelf thinning. Our nominal projections showed that the AIS contribution to sea-level rise by 3000 is rather limited (less than 1 metre) in RCP 2.6, RCP 4.5 and RCP 6.0, while an accelerated ice loss that leads to a contribution of several meters is triggered in RCP 8.5 (Fig. 3a) and that the nominal retreat of the grounding line by 3000 is rather limited in RCP 2.6, RCP 4.5 and RCP 6.0 (Fig. 3b–d), while a significant retreat of the grounding line is triggered in the Siple Coast, Ronne–Filchner and Amundsen Sea

10 sectors in RCP 8.5 (Fig. 3e).

Our probabilistic results provide insight into the impact of parametric uncertainty on these projections. In RCP 2.6, the projections hold irrespectively of parametric uncertainty: the AIS contribution to sea-level rise by 3000 has a 95 % quantile of up to 0.91 m (Table 3) and there is a limited risk that the grounding line retreats beyond our nominal projections (Fig. 3b and Fig. 10c). In RCP 4.5 and RCP 6.0, the projections are more sensitive to parametric uncertainty than in RCP 2.6: the AIS

15 contribution to sea-level rise by 3000 has a 95 % quantile of up to 2.56 m in RCP 4.5 and up to 5.17 m in RCP 6.0 (Table 3) and both scenarios entail a risk of triggering a more significant retreat of the grounding line beyond our nominal projections (Fig. 3c–d). This risk is present especially in the Amundsen Sea sector and it is less significant in RCP 4.5 than in RCP 6.0, in which a complete disintegration of the West Antarctic ice sheet may be triggered (Fig. 10f and i). Finally, in RCP 8.5, our probabilistic results suggest an accelerated ice loss and a significant retreat of the grounding line in West Antarctica, as in our

20 nominal projections: the AIS contribution to sea-level rise by 3000 has an uncertainty range with a 5 % quantile above 0.82 m and a 95 % quantile of up to 7.68 m (Table 3) and there is a high risk of triggering a complete disintegration of the West Antarctic ice sheet (Fig. 10l).

In conclusion, the projections hold irrespectively of parametric uncertainty in the strongly mitigated RCP 2.6 scenario: accommodating parametric uncertainty in the ice-sheet model does not question the nominal projections of limited ice loss and

25 limited grounding-line retreat in RCP 2.6. However, the projections are more sensitive to parametric uncertainty for intermediate scenarios such as RCP 4.5 and RCP 6.0: accommodating parametric uncertainty in the ice-sheet model questions the nominal projections and indicates instead some risk of triggering accelerated ice loss and significant grounding-line retreat for intermediate scenarios such as RCP 4.5 and RCP 6.0. Finally, the warm RCP 8.5 scenario triggers the collapse of the West Antarctic ice sheet, almost irrespectively of parametric uncertainty.

30 4.5 Structural uncertainty and limitations

A first limitation of our study is associated with the modelling hypotheses inherent to our ice-sheet model. The f.ETISh model is an ice-sheet model that focuses on essential marine ice-sheet mechanisms, similarly to the ice-sheet model by Pollard and DeConto (2012a). Certain physical processes, especially small-scale processes, may be represented imperfectly. This may re-

duce the ability to simulate important ice streams such as Pine Island and Thwaites glaciers, whose stability is controlled by local bedrock features (Waibel et al., 2018). Hence, grounding-line migration and thresholds for instabilities may be not captured properly even with grounding-line flux parameterisation, especially in low-forcing scenarios and short-term projections. Despite the use of the PICO ocean coupler, sub-shelf melting may not be appropriately represented especially in the Amund-

5   sen Sea sector and underneath Ross ice shelf. A second limitation comes from the hypotheses relevant to our characterisation of uncertainties. We adopted rather large uncertainty ranges for the parameters. As we showed, projections can be strongly affected by extreme conditions. Moreover, we chose the bounds of the uncertainty ranges quite heuristically. A third limitation comes from the fairly simple way in which certain sources of uncertainty were introduced. We assumed a direct influence of the atmospheric forcing on sub-shelf melting through the ocean melt factor. But, in fact, atmospheric forcing affects the Cir-

10 cumpolar Deep Water circulation in ice-shelf cavities and subsequently modifies sub-shelf melting (Pritchard et al., 2012). We also introduced uncertainty in calving with a simple multiplier factor that does not take into account the stress regime in the ice shelves. Another limitation is related to the construction of our emulator. To avoid overfitting the training data, we tuned the emulator to reproduce the overall trend in the parameters-to-projections relationship but not local variations in the parameter space that may stem from numerical noise and errors.

5   Conclusions

We studied the multi-centennial response of the Antarctic ice sheet under uncertainty using methods from the UQ community. We investigated uncertainties in atmospheric forcing, basal sliding, grounding-line parameterisation, sub-shelf melting, calving, ice-shelf rheology and bedrock relaxation. We used emulation-based methods to represent the parameters-to-projection relationship, stochastic sensitivity analysis to assess the significance of each source of uncertainty in inducing uncertainty in

20 the projections and confidence regions for excursion sets to assess the risk of grounding-line retreat. We found that all sources of uncertainty, except perhaps the bedrock relaxation times, contribute to the uncertainty in the projections. We showed that the sensitivity of the projections to uncertainties increases and the contribution of the uncertainty in sub-shelf melting to the uncertainty in the projections becomes more and more dominant as the scenario gets warmer. We showed that the significance of the AIS contribution to sea-level rise is controlled by MISI in marine basins, with the biggest contribution stemming from

25 the more vulnerable West Antarctic ice sheet. We found that, irrespectively of parametric uncertainty, the strongly mitigated RCP 2.6 scenario prevents the collapse of the West Antarctic ice sheet, that in both RCP 4.5 and RCP 6.0 scenarios the occurrence of MISI in marine basins is more sensitive to parametric uncertainty and that, almost irrespectively of parametric uncertainty, RCP 8.5 triggers the collapse of the West Antarctic ice sheet.

Data availability. All datasets used in this paper are publicly available, including Bedmap2 (Fretwell et al., 2013), ocean temperature and

30 salinity (Schmidtko et al., 2014) and geothermal heat flux (An et al., 2015). Results of the RACMO2 model were kindly provided by

Melchior Van Wessen. Results from the f.ETISh model for this study are available on request from K. Bulthuis (kevin.bulthuis@uliege.be). The MATLAB code used to analyse the results is also available on request from the same author.

Appendix A: Polynomial chaos expansion

In this appendix, we concisely provide further details about how we used PC expansions in our study; we refer the reader to, for instance, Ghanem et al. (2017) and Le Maître and Knio (2010) for more comprehensive treatments of the theory and various applications of PC expansions.

Let us represent the ice-sheet model as an abstract model $y = g(\boldsymbol{x})$ where $\boldsymbol{x} = (x_1, \ldots, x_d)$ is a vector of d parameters, y the model response and g the response function. In our study, $d = 5$, $x_1 = F_{\text{calv}}$, $x_2 = F_{\text{melt}}$, $x_3 = E_{\text{shelf}}$, $x_4 = \tau_{\text{e}}$, $x_5 = \tau_{\text{w}}$ and $y = \Delta\text{GMSL}$ at a given time. In our study, the parameters are uncertain and have a probability density function which we denote by p.

A polynomial chaos expansion is an approximation of the response function g with a polynomial g^K as

$$g(\boldsymbol{x}) \approx g^K(\boldsymbol{x}) = \sum_{k=0}^{K} c_k \psi_k(\boldsymbol{x}), \tag{A1}$$

where the ψ_k are a basis of predefined polynomials of increasing degree and orthonormal with respect to the probability density function of the parameters, by which we understand that

$$\int_{\mathbb{R}^d} \psi_k(\boldsymbol{x}) \psi_l(\boldsymbol{x}) p(\boldsymbol{x}) \, d\boldsymbol{x} = \begin{cases} 0 \text{ if } k \neq l \\ 1 \text{ if } k = l \end{cases}, \tag{A2}$$

and $K + 1$ is the number of predefined polynomials in the expansion.

In order to fit the PC expansion in Eq. (A1) to the ice-sheet model, we calculate the coefficients using a (weighted) least-squares approach:

$$\boldsymbol{c} = \arg \min_{\boldsymbol{d} \in \mathbb{R}^{K+1}} \sum_{i=1}^{N} w^{(i)} \left(y^{(i)} - \sum_{k=0}^{K} d_k \psi_k(\boldsymbol{x}^{(i)}) \right)^2, \tag{A3}$$

where $\{\boldsymbol{x}^{(i)}, 1 \leqslant i \leqslant N\}$ is a set of N training points in the parameter space, $\{y^{(i)} = g(\boldsymbol{x}^{(i)}), 1 \leqslant i \leqslant N\}$ is the set of model responses at the training points, $\boldsymbol{c} = (c_0, c_1, \ldots, c_K)$ collects the PC coefficients and $\{w^{(i)}, 1 \leqslant i \leqslant N\}$ is the set of weights. We normalise the parameters to accommodate the different orders of magnitude of the parameters and reduce the potential ill-conditioning of the least-squares problem. We generate the set of training points with a maximin Latin hypercube sampling design (Stein, 1987; Fajraoui et al., 2017; Hadigol and Doostan, 2018), which is a space-filling design that aims at maximising the smallest distance between neighbouring points, thus ensuring a proper coverage of the parameter space. We consider a PC expansion of degree 3, which correspond to $K = 56$ for $d = 5$, as we strive to reproduce the overall trend of the response function without overfitting small local variations.

We solve Eq. (A3) by solving the normal equations

$$(\mathbf{G}^T \mathbf{W} \mathbf{G}) \boldsymbol{c} = \mathbf{G}^T \mathbf{W} \boldsymbol{y}, \tag{A4}$$

where $\boldsymbol{y} = (y^{(1)}, \ldots, y^{(N)})$ collects the model responses at the training points, $\mathbf{G}$ is the measurement matrix whose entries are given by $\mathbf{G}_{ki} = \psi_k(\boldsymbol{x}^{(i)})$ and $\mathbf{W}$ is a diagonal weight matrix whose diagonal entries are the weights ($\mathbf{W}_{ii} = w^{(i)}$). As we construct the training points by using a Latin hypercube sampling design, the training points $\boldsymbol{x}^{(i)}$ have equal weights of $\mathbf{W}_{ii} = w^{(i)} = 1/N$. We do note that there exist other methods to determine the coefficients in Eq. (A1) including methods

5   involving deterministic quadrature rules (Le Maître and Knio, 2010). Here, one of our motivations for choosing a least-squares approach is its good ability to handle numerical noise in low-degree expansions (Iskandarani et al., 2016).

We estimate statistical descriptors of the uncertain model response with Monte Carlo simulation in which the PC expansion is used as a computationally efficient substitute for the ice-sheet model. For instance, we estimate the probability density function of the response through kernel density estimation (Scott, 2015), while we approximate the mean μ and the variance

10   σ^2 of the model response as

$$\mu \approx \mu^{K,\nu} = \frac{1}{\nu} \sum_{i=1}^{\nu} g^K(\boldsymbol{x}^{(i)}), \tag{A5}$$

$$\sigma^2 \approx \left(\sigma^{K,\nu}\right)^2 = \frac{1}{\nu} \sum_{i=1}^{\nu} \left(g^K(\boldsymbol{x}^{(i)}) - \mu^{K,\nu}\right)^2, \tag{A6}$$

where $\left\{\boldsymbol{x}^{(i)}, 1 \leqslant i \leqslant \nu\right\}$ now denotes an ensemble of ν independent and identically distributed samples from the probability density function of the parameters. Because the PC expansion is based on orthonormal polynomials with respect to the proba-

15   bility density function of the uncertain parameters and of increasing degree with $\psi_0 = 1$, we can evaluate some of the statistical descriptors of the uncertain model response directly from the PC coefficients. For example, the mean μ and the variance σ^2 of the model response can also be approximated as follows

$$\mu \approx \mu^K = c_0, \tag{A7}$$

$$\sigma^2 \approx \left(\sigma^K\right)^2 = \sum_{k=1}^{K} c_k^2. \tag{A8}$$

20   The accuracy of the PC expansion has to be assessed with respect to the degree of the PC expansion and the number of training points. We validate the accuracy of the PC expansion using cross-validation and convergence tests. We generate a new set of samples in the parameter space and we compare the exact response of the ice-sheet model with the approximate response of the PC expansion. Figures A1a–c show results of such a cross-validation for a PC expansion of degree 3. These figures suggest that the PC expansion represents the overall model response with sufficient accuracy. Lower accuracy is achieved near

25   the boundaries of the parameter space. We also carry out convergence tests, as illustrated in Fig. A1d in RCP 8.5 and at time 3000. This figure represents the maximum absolute error and the mean-square error between the exact response of the ice-sheet model and the approximate response of the PC expansion at the training points as a function of the number of training points. We see that for the 500 training points considered in this paper, reasonable convergence of the PC expansion is achieved.

Appendix B: Sobol sensitivity indices

In this appendix, we concisely provide further details about how we used stochastic sensitivity analysis; we refer the reader to, for instance, Ghanem et al. (2017) and Saltelli et al. (2008) for more comprehensive treatments of the theory and various applications.

Assuming that the uncertain parameters are statistically independent, Sobol indices are based on the decomposition of the response function g in terms of the main effects associated with the parameters individually and an interaction effect associated with all parameters together:

$$y = g(\boldsymbol{x}) = g_0 + \sum_{i=1}^{d} g_i(x_i) + g_I(\boldsymbol{x}), \tag{B1}$$

where g_0 is constant, each g_i the so-called main effect associated with the corresponding parameter x_i and g_I the so-called interaction effect. The constant and the main effects are defined by

$$g_0 = \int_{\mathbb{R}^d} g(\boldsymbol{x})p(\boldsymbol{x})\,d\boldsymbol{x}, \tag{B2}$$

$$g_i = \int_{\mathbb{R}^{d-1}} g(\boldsymbol{x})p_{-i}(\boldsymbol{x}_{-i})\,d\boldsymbol{x}_{-i} - g_0, \ 1 \leqslant i \leqslant d, \tag{B3}$$

where $\boldsymbol{x}_{-i} = (x_1, \ldots, x_{i-1}, x_{i+1}, \ldots, x_d)$ denotes the subset of parameters including all the parameters except x_i and p_{-i} denotes the probability density function for this subset of parameters. The constant g_0 is the mean value of g. Using the calculus of variations, it can be shown that the main effect g_i is such that the function $g_0 + g_i$ is the least-squares best approximation of g among all functions that depend only on x_i. As a consequence of this least-squares best approximation property, the functions $g_0, g_1, \ldots, g_d, g_I$ are orthonormal with respect to the probability density function of the uncertain parameter.

As a consequence of the orthonormality of the functions $g_0, g_1, \ldots, g_d, g_I$, the variance σ^2 of the model response can be decomposed as

$$\sigma^2 = \left(\sum_{i=1}^{d} S_i + S_I \right) \sigma^2, \tag{B4}$$

where

$$S_i = \frac{1}{\sigma^2} \int_{\mathbb{R}} |g_i(x_i)|^2 p_i(x_i)\,dx_i, \ 1 \leqslant i \leqslant d, \tag{B5}$$

in which p_i denotes the probability density function for x_i. Here, S_i, which takes a value between 0 and 1, is the Sobol index for the i-th parameter and S_I is the interaction index. The Sobol index S_i can be interpreted either as the relative contribution of the uncertainty in the sole i-th parameter to the variance of the model response or as the reduction in the variance of the model response that we may expect by learning the exact value of this parameter (Oakley and O'Hagan, 2004). Sobol indices allow to rank the uncertain parameters in terms of their contribution to the variance of the model response, thus indicating which parameters are most influential in inducing the uncertainty in the model response.

Here, we substituted the ice-sheet model by a PC expansion based on orthonormal polynomials and estimated the Sobol indices directly from the PC coefficients (Crestaux et al., 2009), that is,

$$S_i \approx S_i^K = \frac{1}{\left(\sigma^K\right)^2} \sum_{k \in A_i} c_k^2, \tag{B6}$$

where A_i is the set of indices associated with the non-constant polynomials that only depend on x_i.

5 Appendix C: Confidence regions for grounded ice

In this appendix, we concisely provide further details about how we defined and computed confidence regions for grounded ice. To distinguish between grounded ice and floating ice at a given time, the f.ETISh model (Pattyn, 2017) evaluates the so-called buoyancy imbalance

$$BI(\boldsymbol{x}) = \rho_w b(\boldsymbol{x}) + \rho_i h(\boldsymbol{x}), \tag{C1}$$

10 where b is the bedrock elevation, h the ice thickness, ρ_w the water density and ρ_i the ice density. The buoyancy imbalance is negative for floating ice, positive for grounded ice and null at the grounding line. Therefore, the grounded ice domain D_g is

$$D_g = \{\boldsymbol{x} : BI(\boldsymbol{x}) \geqslant 0\}. \tag{C2}$$

In the presence of uncertainties in the model, we define an α % confidence region $D_g(\alpha)$ for the grounded ice domain as a subregion of Antarctica that has a probability of at least α to be included in the grounded ice domain, that is,

15 $$P\{D_g(\alpha) \subseteq D_g\} \geqslant \alpha. \tag{C3}$$

We compute the confidence regions using an adaptation of a thresholding algorithm by Bolin and Lindgren (2015). We seek the confidence regions in a parametric family indexed by a threshold parameter and based on the marginal probability density functions and we determine the threshold parameter so as to achieve the required level of confidence. While Bolin and Lindgren (2015) consider Gaussian random fields, here we work with non-Gaussian random fields, which requires to evaluate

20 the marginal probability density functions and the probability of inclusion with Monte-Carlo simulation.

Author contributions. All authors discussed the results presented in this manuscript. KB conducted the design, execution and UQ analysis of the experiments with relevant inputs from MA for the UQ methodology and SS and FP for the physical interpretation of the results. The manuscript was written by KB and MA with relevant comments from all co-authors

Competing interests. The authors declare that they have no conflict of interest.

Acknowledgements. K. Bulthuis would like to acknowledge the Fonds de la Recherche Scientifique de Belgique (F.R.S.-FNRS) for its financial support (F.R.S.-FNRS Research Fellowship). Computational resources have been provided by the Consortium des Équipements de Calcul Intensif (CÉCI), funded by the Fonds de la Recherche Scientifique de Belgique (F.R.S-FNRS) under Grant No.2.5020.11.

References

Adhikari, S., Ivins, E. R., Larour, E., Seroussi, H., Morlighem, M., and Nowicki, S.: Future Antarctic bed topography and its implications for ice sheet dynamics, Solid Earth, 5, 569–584, https://doi.org/10.5194/se-5-569-2014, 2014.

An, M., Wiens, D. A., Zhao, Y., Feng, M., Nyblade, A., Kanao, M., Li, Y., Maggi, A., and Lévêque, J.-J.: Temperature, lithosphere-asthenosphere boundary, and heat flux beneath the Antarctic Plate inferred from seismic velocities, J. Geophys. Res.: Solid Earth, 120, 8720–8742, https://doi.org/10.1002/2015jb011917, 2015.

Arnst, M. and Ponthot, J.-P.: An overview of nonintrusive characterization, propagation, and sensitivity analysis of uncertainties in computational mechanics, Int. J. Uncertain. Quantif., 4, 387–421, https://doi.org/10.1615/int.j.uncertaintyquantification.2014006990, 2014.

Arthern, R. J. and Williams, C. R.: The sensitivity of West Antarctica to the submarine melting feedback, Geophys. Res. Lett., 45, 809–816, https://doi.org/10.1002/2017gl072514, 2017.

Barletta, V. R., Bevis, M., Smith, B. E., Wilson, T., Brown, A., Bordoni, A., Willis, M., Khan, S. A., Rovira-Navarro, M., Dalziel, I., Smalley, Jr., R., Kendrick, E., Konfal, S., Caccamise II, D. J., Aster, R. C., Nyblade, A., and Wiens, D. A.: Observed rapid bedrock uplift in Amundsen Sea Embayment promotes ice-sheet stability, Science, 360, 1335–1339, https://doi.org/10.1126/science.aao1447, 2018.

Bennett, M. R.: Ice streams as the arteries of an ice sheet: their mechanics, stability and significance, Earth-Sci. Rev., 61, 309–339, https://doi.org/10.1016/s0012-8252(02)00130-7, 2003.

Bindschadler, R. A., Nowicki, S., Abe-Ouchi, A., Aschwanden, A., Choi, H., Fastook, J., Granzow, G., Greve, R., Gutowski, G., Herzfeld, U., Jackson, C., Johnson, J., Khroulev, C., Levermann, A., Lipscomb, W. H., Martin, M. A., Morlighem, M., Parizek, B. R., Pollard, D., Price, S. F., Ren, D., Saito, F., Sato, T., Seddik, H., Seroussi, H., Takahashi, K., Walker, R., and Wang, W. L.: Ice-sheet model sensitivities to environmental forcing and their use in projecting future sea level (the SeaRISE project), J. Glaciol., 59, 195–224, https://doi.org/10.3189/2013jog12j125, 2013.

Bolin, D. and Lindgren, F.: Excursion and contour uncertainty regions for latent Gaussian models, J. Royal Stat. Soc. B, 77, 85–106, https://doi.org/10.1111/rssb.12055, 2015.

Briggs, R., Pollard, D., and Tarasov, L.: A glacial systems model configured for large ensemble analysis of Antarctic deglaciation, The Cryosphere, 7, 1949–1970, https://doi.org/10.5194/tc-7-1949-2013, 2013.

Brondex, J., Gagliardini, O., Gillet-Chaulet, F., and Durand, G.: Sensitivity of grounding line dynamics to the choice of the friction law, J. Glaciol., 63, 854–866, https://doi.org/10.1017/jog.2017.51, 2017.

Bueler, E. and Brown, J.: Shallow shelf approximation as a "sliding law" in a thermomechanically coupled ice sheet model, J. Geophys. Res., 114, https://doi.org/10.1029/2008jf001179, 2009.

Calonne, N., Montagnat, M., Matzl, M., and Schneebeli, M.: The layered evolution of fabric and microstructure of snow at Point Barnola, Central East Antarctica, Earth Planet. Sci. Lett., 460, 293–301, https://doi.org/10.1016/j.epsl.2016.11.041, 2017.

Chen, B., Haeger, C., Kaban, M. K., and Petrunin, A. G.: Variations of the effective elastic thickness reveal tectonic fragmentation of the Antarctic lithosphere, Tectonophysics, https://doi.org/10.1016/j.tecto.2017.06.012, in Press, 2017.

Conrad, P. R., Davis, A. D., Marzouk, Y. M., Pillai, N. S., and Smith, A.: Parallel Local Approximation MCMC for Expensive Models, SIAM/ASA JUQ, 6, 339–373, https://doi.org/10.1137/16m1084080, 2018.

Cornford, S. L., Martin, D. F., Payne, A. J., Ng, E. G., Brocq, A. M. L., Gladstone, R. M., Edwards, T. L., Shannon, S. R., Agosta, C., van den Broeke, M. R., Hellmer, H. H., Krinner, G., Ligtenberg, S. R. M., Timmermann, R., and Vaughan, D. G.: Century-scale simulations of the

response of the West Antarctic Ice Sheet to a warming climate, The Cryosphere, 9, 1579–1600, https://doi.org/10.5194/tc-9-1579-2015, 2015.

Crestaux, T., Le Maître, O., and Martinez, J.-M.: Polynomial chaos expansion for sensitivity analysis, Reliab. Eng. Syst. Safe., 94, 1161–1172, https://doi.org/10.1016/j.ress.2008.10.008, 2009.

5 DeConto, R. M. and Pollard, D.: Contribution of Antarctica to past and future sea-level rise, Nature, 531, 591–597, https://doi.org/10.1038/nature17145, 2016.

Depoorter, M. A., Bamber, J. L., Griggs, J. A., Lenaerts, J. T. M., Ligtenberg, S. R. M., van den Broeke, M. R., and Moholdt, G.: Calving fluxes and basal melt rates of Antarctic ice shelves, Nature, 502, 89–92, https://doi.org/10.1038/nature12567, 2013.

Fajraoui, N., Marelli, S., and Sudret, B.: Sequential Design of Experiment for Sparse Polynomial Chaos Expansions, SIAM/ASA JUQ, 5,
10 1061–1085, https://doi.org/10.1137/16m1103488, 2017.

Favier, L., Durand, G., Cornford, S. L., Gudmundsson, G. H., Gagliardini, O., Gillet-Chaulet, F., Zwinger, T., Payne, A. J., and Brocq, A. M. L.: Retreat of Pine Island Glacier controlled by marine ice-sheet instability, Nat. Clim. Change, 4, 117–121, https://doi.org/10.1038/nclimate2094, 2014.

Fretwell, P., Pritchard, H. D., Vaughan, D. G., Bamber, J. L., Barrand, N. E., Bell, R., Bianchi, C., Bingham, R. G., Blankenship, D. D.,
15 Casassa, G., Catania, G., Callens, D., Conway, H., Cook, A. J., Corr, H. F. J., Damaske, D., Damm, V., Ferraccioli, F., Forsberg, R., Fujita, S., Gogineni, P., Griggs, J. A., Hindmarsh, R. C. A., Holmlund, P., Holt, J. W., Jacobel, R. W., Jenkins, A., Jokat, W., Jordan, T., King, E. C., Kohler, J., Krabill, W., Riger-Kusk, M., Langley, K. A., Leitchenkov, G., Leuschen, C., Luyendyk, B. P., Matsuoka, K., Nogi, Y., Nost, O. A., Popov, S. V., Rignot, E., Rippin, D. M., Riviera, A., Roberts, J., Ross, N., Siegert, M. J., Smith, A. M., Steinhage, D., Studinger, M., Sun, B., Tinto, B. K., Welch, B. C., Young, D. A., Xiangbin, C., and Zirizzotti, A.: Bedmap2: improved ice bed, surface
20 and thickness datasets for Antarctica, The Cryosphere, 7, 375–393, https://doi.org/10.5194/tc-7-375-2013, 2013.

Ghanem, R., Higdon, R., and Owhadi, H., eds.: Handbook of Uncertainty Quantification, Springer, https://doi.org/10.1007/978-3-319-12385-1, 2017.

Ghanem, R. G. and Spanos, P. D.: Stochastic Finite Elements: A Spectral Approach, Dover Publications, Mineola, New York, revised edn., 2003.

25 Gillet-Chaulet, F., Durand, G., Gagliardini, O., Mosbeux, C., Mouginot, J., Rémy, F., and Ritz, C.: Assimilation of surface velocities acquired between 1996 and 2010 to constrain the form of the basal friction law under Pine Island Glacier, Geophys. Res. Lett., 43, 10,311–10,321, https://doi.org/10.1002/2016gl069937, 2016.

Goelzer, H., Nowicki, S., Edwards, T., Beckley, M., Abe-Ouchi, A., Aschwanden, A., Calov, R., Gagliardini, O., Gillet-Chaulet, F., Golledge, N. R., Gregory, J., Greve, R., Humbert, A., Huybrechts, P., Kennedy, J. H., Larour, E., Lipscomb, W. H., clec'h, S. L., Lee, V., Morlighem,
30 M., Pattyn, F., Payne, A. J., Rodehacke, C., Rückamp, M., Saito, F., Schlegel, N., Seroussi, H., Shepherd, A., Sun, S., van de Wal, R., and Ziemen, F. A.: Design and results of the ice sheet model initialisation experiments initMIP-Greenland: an ISMIP6 intercomparison, The Cryosphere, 12, 1433–1460, https://doi.org/10.5194/tc-12-1433-2018, 2018.

Golledge, N. R., Kowalewski, D. E., Naish, T. R., Levy, R. H., Fogwill, C. J., and Gasson, E. G. W.: The multi-millennial Antarctic commitment to future sea-level rise, Nature, 526, 421–425, https://doi.org/10.1038/nature15706, 2015.

35 Golledge, N. R., Levy, R. H., McKay, R. M., and Naish, T. R.: East Antarctic ice sheet most vulnerable to Weddell Sea warming, Geophys. Res. Lett., 44, 2343–2351, https://doi.org/10.1002/2016gl072422, 2017.

Gomez, N., Mitrovica, J. X., Huybers, P., and Clark, P. U.: Sea level as a stabilizing factor for marine-ice-sheet grounding lines, Nat. Geosci., 3, 850–853, https://doi.org/10.1038/ngeo1012, 2010.

Gomez, N., Pollard, D., and Mitrovica, J. X.: A 3-D coupled ice sheet – sea level model applied to Antarctica through the last 40 ky, Earth Planet. Sci. Lett., 384, 88–99, https://doi.org/10.1016/j.epsl.2013.09.042, 2013.

Gopalan, G., Hrafnkelsson, B., Aðalgeirsdóttir, G., Jarosch, A. H., and Pálsson, F.: A Bayesian hierarchical model for glacial dynamics based on the shallow ice approximation and its evaluation using analytical solutions, The Cryosphere, 12, 2229–2248, https://doi.org/10.5194/tc-12-2229-2018, 2018.

Greve, R. and Blatter, H.: Dynamics of Ice Sheets and Glaciers, Advances in Geophysical and Environmental Mechanics and Mathematics, Springer-Verlag Berlin Heidelberg, https://doi.org/10.1007/978-3-642-03415-2, 2009.

Hadigol, M. and Doostan, A.: Least squares polynomial chaos expansion: A review of sampling strategies, Comput. Methods Appl. Mech. Eng., 332, 382–407, https://doi.org/10.1016/j.cma.2017.12.019, 2018.

Huybrechts, P., Abe-Ouchi, A., Marsiat, I., Pattyn, F., Payne, T., Ritz, C., and Rommelaere, V.: Report of the Third EISMINT Workshop on Model Intercomparison, European Science Foundation (Strasbourg), 1998.

Isaac, T., Petra, N., Stadler, G., and Ghattas, O.: Scalable and efficient algorithms for the propagation of uncertainty from data through inference to prediction for large-scale problems, with application to flow of the Antarctic ice sheet, J. Comput. Phys., 296, 348–368, https://doi.org/10.1016/j.jcp.2015.04.047, 2015.

Iskandarani, M., Wang, S., Srinivasan, A., Thacker, W. C., Winokur, J., and Knio, O. M.: An overview of uncertainty quantification techniques with application to oceanic and oil-spill simulations, J. Geophys. Res.: Oceans, 121, 2789–2808, https://doi.org/10.1002/2015jc011366, 2016.

Janssens, I. and Huybrechts, P.: The treatment of meltwater retention in mass-balance parameterizations of the Greenland ice sheet, Ann. Glaciol., 31, 133–140, https://doi.org/10.3189/172756400781819941, 2000.

Joughin, I., Tulaczyk, S., Bamber, J. L., Blankenship, D., Holt, J. W., Scambos, T., and Vaughan, D. G.: Basal conditions for Pine Island and Thwaites Glaciers, West Antarctica, determined using satellite and airborne data, J. Glaciol., 55, 245–257, https://doi.org/10.3189/002214309788608705, 2009.

Joughin, I., Smith, B. E., and Holland, D. M.: Sensitivity of 21st century sea level to ocean-induced thinning of Pine Island Glacier, Antarctica, Geophys. Res. Lett., 37, https://doi.org/10.1029/2010gl044819, 2010.

Joughin, I., Smith, B. E., and Medley, B.: Marine Ice Sheet Collapse Potentially Under Way for the Thwaites Glacier Basin, West Antarctica, Science, 344, 735–738, https://doi.org/10.1126/science.1249055, 2014.

Knutti, R., Furrer, R., Tebaldi, C., Cermak, J., and Meehl, G. A.: Challenges in Combining Projections from Multiple Climate Models, J. Climate, 23, 2739–2758, https://doi.org/10.1175/2009jcli3361.1, 2010.

Le Gratiet, L., Marelli, S., and Sudret, B.: Metamodel-Based Sensitivity Analysis: Polynomial Chaos Expansions and Gaussian Processes, in: Handbook of Uncertainty Quantification, edited by Ghanem, R., Higdon, R., and Owhadi, H., chap. 38, pp. 1289–1325, Springer, 2017.

Le Maître, O. P. and Knio, O. M.: Spectral Methods for Uncertainty Quantification: With Applications to Computational Fluid Dynamics, Springer Science & Business Media, https://doi.org/10.1007/978-90-481-3520-2, 2010.

Ma, Y., Gagliardini, O., Ritz, C., Gillet-Chaulet, F., Durand, G., and Montagnat, M.: Enhancement factors for grounded ice and ice shelves inferred from an anisotropic ice-flow model, J. Glaciol., 56, 805–812, https://doi.org/10.3189/002214310794457209, 2010.

Maris, M. N. A., de Boer, B., Ligtenberg, S. R. M., Crucifix, M., van de Berg, W. J., and Oerlemans, J.: Modelling the evolution of the Antarctic ice sheet since the last interglacial, The Cryosphere, 8, 1347–1360, https://doi.org/10.5194/tc-8-1347-2014, 2014.

Nowicki, S. M. J., Payne, A., Larour, E., Seroussi, H., Goelzer, H., Lipscomb, W., Gregory, J., Abe-Ouchi, A., and Shepherd, A.: Ice Sheet Model Intercomparison Project (ISMIP6) contribution to CMIP6, Geosci. Model Dev., 9, 4521–4545, https://doi.org/10.5194/gmd-9-4521-2016, 2016.

Oakley, J. E. and O'Hagan, A.: Probabilistic sensitivity analysis of complex models: a Bayesian approach, J. Royal Stat. Soc. B, 66, 751–769,
5   https://doi.org/10.1111/j.1467-9868.2004.05304.x, 2004.

Pattyn, F.: Sea-level response to melting of Antarctic ice shelves on multi-centennial timescales with the fast Elementary Thermomechanical Ice Sheet model (f.ETISh v1.0), The Cryosphere, 11, 1851–1878, https://doi.org/10.5194/tc-11-1851-2017, 2017.

Pattyn, F., Schoof, C., Perichon, L., Hindmarsh, R. C. A., Bueler, E., de Fleurian, B., Durand, G., Gagliardini, O., Gladstone, R., Goldberg, D., Gudmundsson, G. H., Huybrechts, P., Lee, V., Nick, F. M., Payne, A. J., Pollard, D., Rybak, O., Saito, F., and Vieli, A.: Results of the
10   Marine Ice Sheet Model Intercomparison Project, MISMIP, The Cryosphere, 6, 573–588, https://doi.org/10.5194/tc-6-573-2012, 2012.

Pattyn, F., Perichon, L., Durand, G., Favier, L., Gagliardini, O., Hindmarsh, R. C., Zwinger, T., Albrecht, T., Cornford, S., Docquier, D., Fürst, J. J., Goldberg, D., Gudmundsson, G. H., Humbert, A., Hütten, M., Huybrechts, P., Jouvet, G., Kleiner, T., Larour, E., Martin, D., Morlighem, M., Payne, A. J., Pollard, D., Rückamp, M., Rybak, O., Seroussi, H., Thoma, M., and Wilkens, N.: Grounding-line migration in plan-view marine ice-sheet models: results of the ice2sea MISMIP3d intercomparison, J. Glaciol., 59, 410–422,
15   https://doi.org/10.3189/2013jog12j129, 2013.

Pattyn, F., Favier, L., Sun, S., and Durand, G.: Progress in Numerical Modeling of Antarctic Ice-Sheet Dynamics, Curr. Clim. Change Rep., 3, 174–184, https://doi.org/10.1007/s40641-017-0069-7, 2017.

Petra, N., Martin, J., Stadler, G., and Ghattas, O.: A Computational Framework for Infinite-Dimensional Bayesian Inverse Problems, Part II: Stochastic Newton MCMC with Application to Ice Sheet Flow Inverse Problems, SIAM J. Sci. Comput., 36, A1525–A1555,
20   https://doi.org/10.1137/130934805, 2014.

Pollard, D. and DeConto, R. M.: Modelling West Antarctic ice sheet growth and collapse through the past five million years, Nature, 458, 329–332, https://doi.org/10.1038/nature07809, 2009.

Pollard, D. and DeConto, R. M.: Description of a hybrid ice sheet-shelf model, and application to Antarctica, Geosci. Model Dev., 5, 1273–1295, https://doi.org/10.5194/gmd-5-1273-2012, 2012a.

25   Pollard, D. and DeConto, R. M.: A simple inverse method for the distribution of basal sliding coefficients under ice sheets, applied to Antarctica, The Cryosphere, 6, 953–971, https://doi.org/10.5194/tc-6-953-2012, 2012b.

Pollard, D., DeConto, R. M., and Alley, R. B.: Potential Antarctic Ice Sheet retreat driven by hydrofracturing and ice cliff failure, Earth Planet. Sci. Lett., 412, 112–121, https://doi.org/10.1016/j.epsl.2014.12.035, 2015.

Pollard, D., Chang, W., Haran, M., Applegate, P., and DeConto, R.: Large ensemble modeling of the last deglacial retreat of the West
30   Antarctic Ice Sheet: comparison of simple and advanced statistical techniques, Geoscientific Model Development, 9, 1697–1723, https://doi.org/10.5194/gmd-9-1697-2016, 2016.

Pritchard, H. D., Ligtenberg, S. R. M., Fricker, H. A., Vaughan, D. G., van den Broeke, M. R., and Padman, L.: Antarctic ice-sheet loss driven by basal melting of ice shelves, Nature, 484, 502–505, https://doi.org/10.1038/nature10968, 2012.

Rasmussen, C. E. and Williams, C. K. I.: Gaussian Processes for Machine Learning, Adaptive computation and machine learning, MIT Press,
35   Cambridge, Massachussetts, 2006.

Reese, R., Albrecht, T., Mengel, M., Asay-Davis, X., and Winkelmann, R.: Antarctic sub-shelf melt rates via PICO, The Cryosphere, 12, 1969–1985, https://doi.org/10.5194/tc-12-1969-2018, 2018.

Rignot, E., Jacobs, S., Mouginot, J., and Scheuchl, B.: Ice-Shelf Melting Around Antarctica, Science, 341, 266–270, https://doi.org/10.1126/science.1235798, 2013.

Rignot, E., Mouginot, J., Morlighem, M., Seroussi, H., and Scheuchl, B.: Widespread, rapid grounding line retreat of Pine Island, Thwaites, Smith, and Kohler glaciers, West Antarctica, from 1992 to 2011, Geophys. Res. Lett., 41, 3502–3509, https://doi.org/10.1002/2014gl060140, 2014.

Ritz, C., Edwards, T. L., Durand, G., Payne, A. J., Peyaud, V., and Hindmarsh, R. C. A.: Potential sea-level rise from Antarctic ice-sheet instability constrained by observations, Nature, 528, 115–118, https://doi.org/10.1038/nature16147, 2015.

Robert, C. P. and Casella, G.: Monte Carlo Statistical Methods, Springer Texts in Statistics, Springer Science & Business Media, 2nd edn., 2013.

Rommelaere, V. and Ritz, C.: A thermomechanical model of ice-shelf flow, Ann. Glaciol., 23, 13–20, https://doi.org/10.3189/s0260305500013203, 1996.

Ruckert, K. L., Shaffer, G., Pollard, D., Guan, Y., Wong, T. E., Forest, C. E., and Keller, K.: Assessing the Impact of Retreat Mechanisms in a Simple Antarctic Ice Sheet Model Using Bayesian Calibration, PLOS ONE, 12, e0170 052, https://doi.org/10.1371/journal.pone.0170052, 2017.

Saltelli, A., Ratto, M., Andres, T., Campolongo, F., Cariboni, J., Gatelli, D., Saisana, M., and Tarantola, S.: Global Sensitivity Analysis: The Primer, John Wiley & Sons, West Sussex, United Kingdom, 2008.

Schlegel, N.-J., Seroussi, H., Schodlok, M. P., Larour, E. Y., Boening, C., Limonadi, D., Watkins, M. M., Morlighem, M., and van den Broeke, M. R.: Exploration of Antarctic Ice Sheet 100-year contribution to sea level rise and associated model uncertainties using the ISSM framework, The Cryosphere, 12, 3511–3534, https://doi.org/10.5194/tc-12-3511-2018, 2018.

Schmidtko, S., Heywood, K. J., Thompson, A. F., and Aoki, S.: Multidecadal warming of Antarctic waters, Science, 346, 1227–1231, https://doi.org/10.1126/science.1256117, 2014.

Schoof, C.: Ice sheet grounding line dynamics: Steady states, stability and hysteresis, J. Geophys. Res., 112, https://doi.org/10.1029/2006JF000664, 2007.

Schoof, C., Davis, A. D., and Popa, T. V.: Boundary layer models for calving marine outlet glaciers, The Cryosphere, 11, 2283–2303, https://doi.org/10.5194/tc-11-2283-2017, 2017.

Scott, D. W.: Multivariate Density Estimation: : Theory, Practice, and Visualization, John Wiley & Sons, 2nd edn., https://doi.org/10.1002/9781118575574, 2015.

Shepherd, A., Ivins, E., Rignot, E., Smith, B., van den Broeke, M., Velicogna, I., Whitehouse, P., Briggs, K., Joughin, I., Krinner, G., Nowicki, S., Payne, T., Scambos, T., Schlegel, N., A, G., Agosta, C., Ahlstrøm, A., Babonis, G., Barletta, V., Blazquez, A., Bonin, J., Csatho, B., Cullather, R., Felikson, D., Fettweis, X., Forsberg, R., Gallee, H., Gardner, A., Gilbert, L., Groh, A., Gunter, B., Hanna, E., Harig, C., Helm, V., Horvath, A., Horwath, M., Khan, S., Kjeldsen, K. K., Konrad, H., Langen, P., Lecavalier, B., Loomis, B., Luthcke, S., McMillan, M., Melini, D., Mernild, S., Mohajerani, Y., Moore, P., Mouginot, J., Moyano, G., Muir, A., Nagler, T., Nield, G., Nilsson, J., Noel, B., Otosaka, I., Pattle, M. E., Peltier, W. R., Pie, N., Rietbroek, R., Rott, H., Sandberg-Sørensen, L., Sasgen, I., Save, H., Scheuchl, B., Schrama, E., Schröder, L., Seo, K.-W., Simonsen, S., Slater, T., Spada, G., Sutterley, T., Talpe, M., Tarasov, L., van de Berg, W. J., van der Wal, W., van Wessem, M., Vishwakarma, B. D., Wiese, D., and Wouters, B.: Mass balance of the Antarctic Ice Sheet from 1992 to 2017, Nature, 558, 219–222, https://doi.org/10.1038/s41586-018-0179-y, 2018.

Stein, M.: Large Sample Properties of Simulations Using Latin Hypercube Sampling, Technometrics, 29, 143–151, https://doi.org/10.2307/1269769, 1987.

Stocker, T. F., Qin, D., Plattner, G.-K., Tignor, M., Allen, S. K., Boshung, J., Nauels, A., Xia, Y., Bex, V., and Midgley, P. M., eds.: Climate Change 2013: The Physical Science Basis. Contribution of Working Group I to the Fifth Assessment Report of the Intergovernmental Panel on Climate Change, Cambridge University Press, Cambridge, United Kingdom and New York, NY, USA, https://doi.org/10.1017/cbo9781107415324, 2013.

5 Taylor, K. E., Stouffer, R. J., and Meehl, G. A.: An Overview of CMIP5 and the Experiment Design, Bull. Am. Meteorol. Soc., 93, 485–498, https://doi.org/10.1175/bams-d-11-00094.1, 2012.

Tsai, V. C., Stewart, A. L., and Thompson, A. F.: Marine ice-sheet profiles and stability under Coulomb basal conditions, J. Glaciol., 61, 205–215, https://doi.org/10.3189/2015jog14j221, 2015.

van der Wal, W., Whitehouse, P. L., and Schrama, E. J.: Effect of GIA models with 3D composite mantle viscosity on GRACE mass balance
10   estimates for Antarctica, Earth Planet. Sci. Lett., 414, 134–143, https://doi.org/10.1016/j.epsl.2015.01.001, 2015.

Waibel, M. S., Hulbe, C. L., Jackson, C. S., and Martin, D. F.: Rate of Mass Loss Across the Instability Threshold for Thwaites Glacier Determines Rate of Mass Loss for Entire Basin, Geophys. Res. Lett., 45, 809–816, https://doi.org/10.1002/2017gl076470, 2018.

Wessem, J. V., Reijmer, C., Morlighem, M., Mouginot, J., Rignot, E., Medley, B., Joughin, I., Wouters, B., Depoorter, M., Bamber, J., Lenaerts, J., Berg, W. V. D., Broeke, M. V. D., and Meijgaard, E. V.: Improved representation of East Antarctic surface mass balance in a
15   regional atmospheric climate model, J. Glaciol., 60, 761–770, https://doi.org/10.3189/2014jog14j051, 2014.

Figures

(a)

(b)
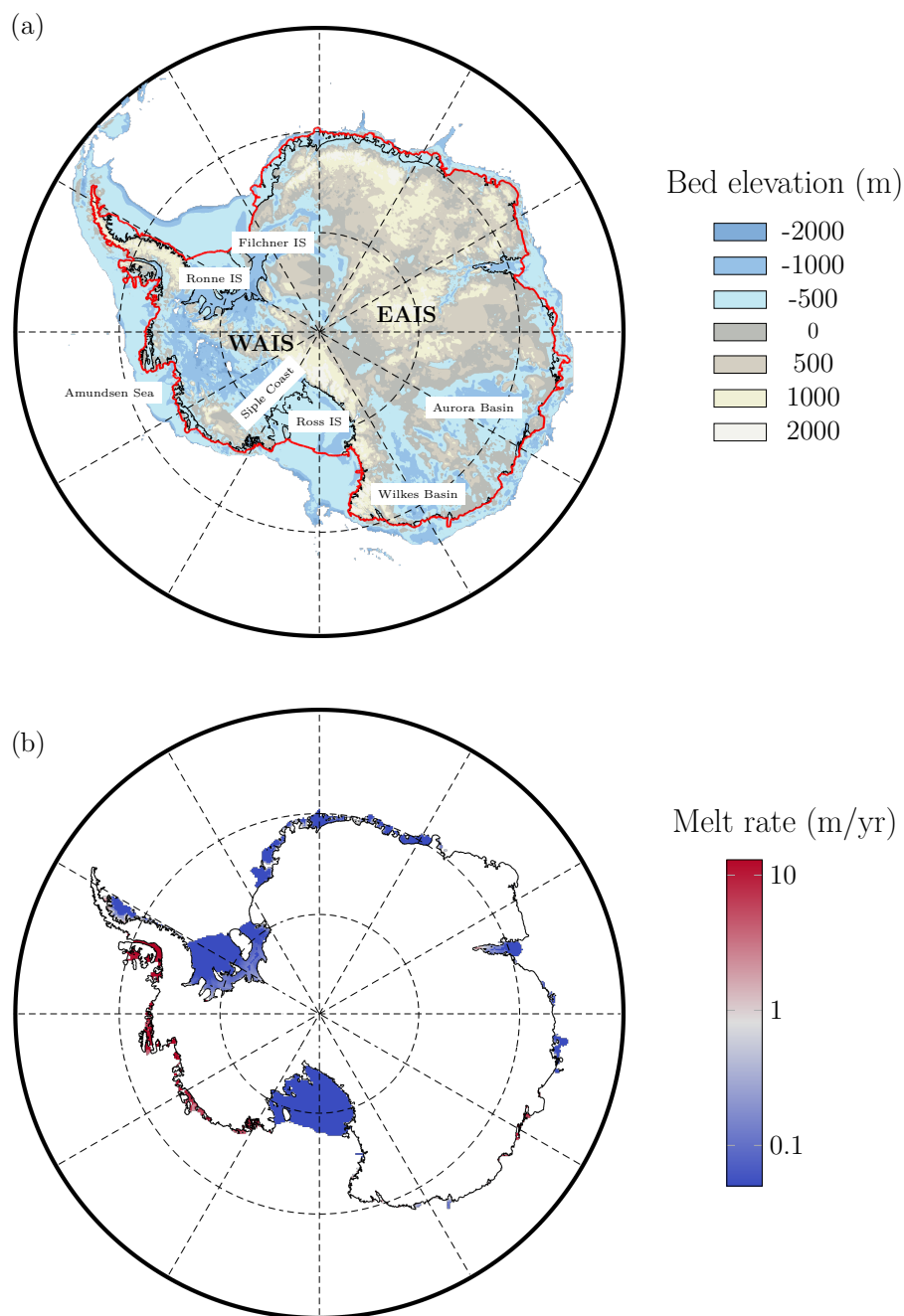
Figure 1. Antarctic bedrock topography and sub-shelf melting. (**a**) Bedrock topography (m a.s.l.) (Fretwell et al., 2013) of present-day Antarctic ice sheet and geographic features. WAIS is West Antarctic ice sheet, EAIS is East Antarctic ice sheet and IS is ice shelf. Grounding line is shown in black and ice front is shown in red. (**b**) Sub-shelf melt rate for present-day Antarctic ice sheet computed with the PICO ocean model (Reese et al., 2018). Refreezing under large shelves is neglected.
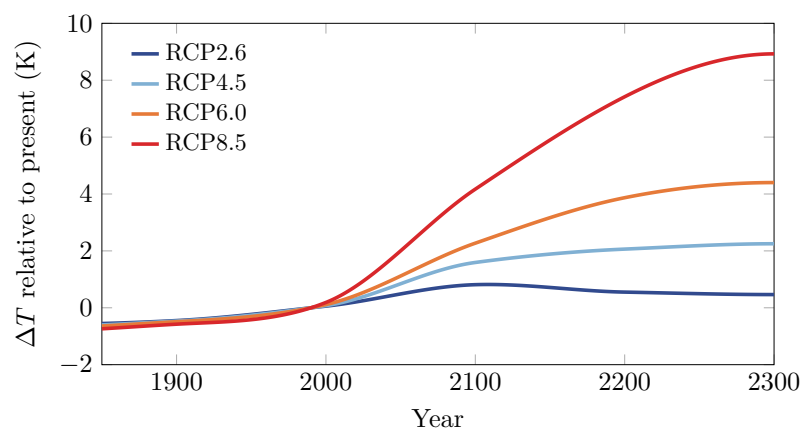
Figure 2. Long-term RCP temperature scenarios (Golledge et al., 2015) for Antarctica (60°-90° S) based on the CMIP5 data (Taylor et al., 2012) and extended to 2300. Temperatures are held constant after 2300.
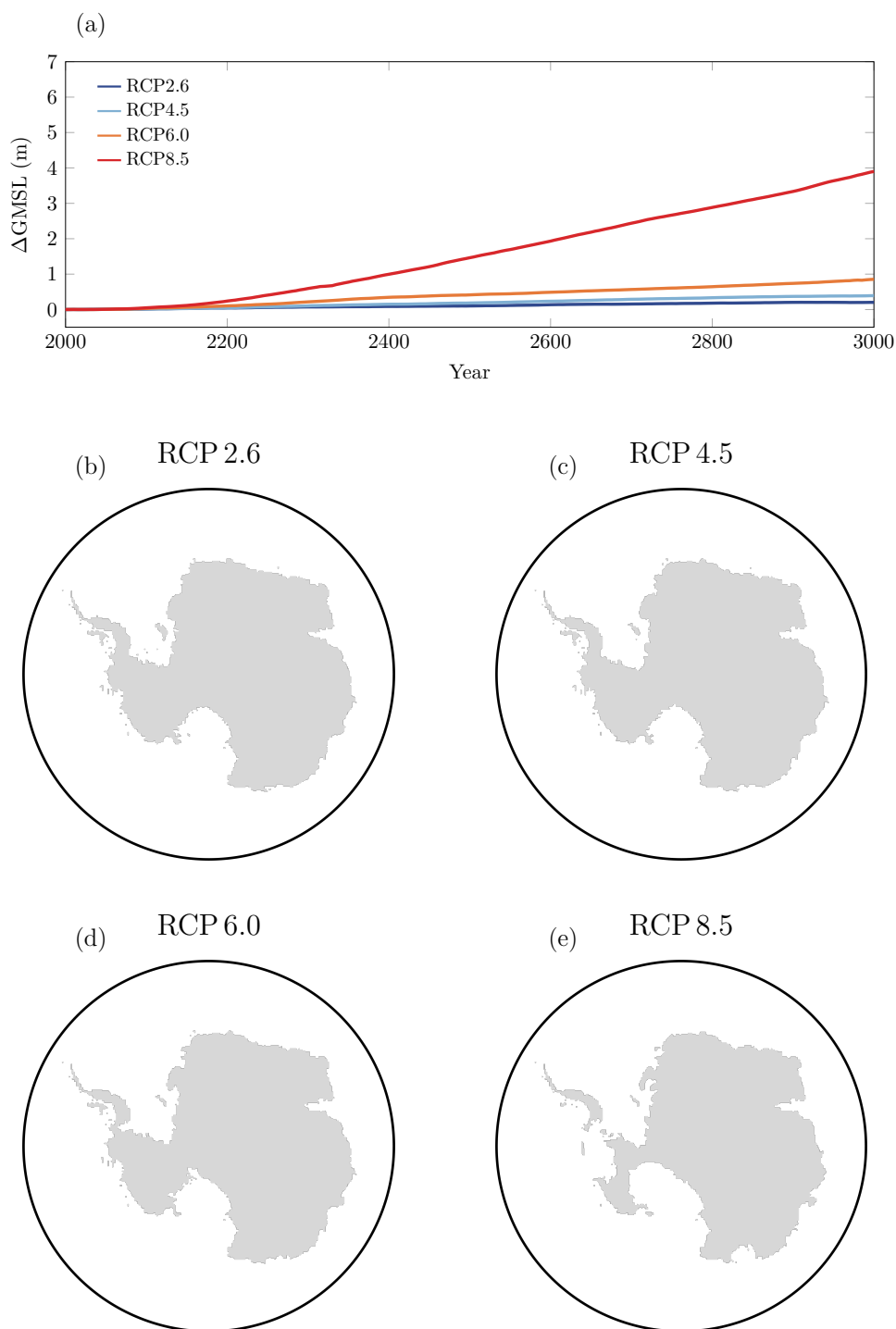
Figure 3. (**a**) Nominal AIS contribution to sea-level rise. Grounded ice (grey area) by 3000 in (**b**) RCP 2.6, (**c**) RCP 4.5, (**d**) RCP 6.0 and (**e**) RCP 8.5 for the nominal values of the parameters.
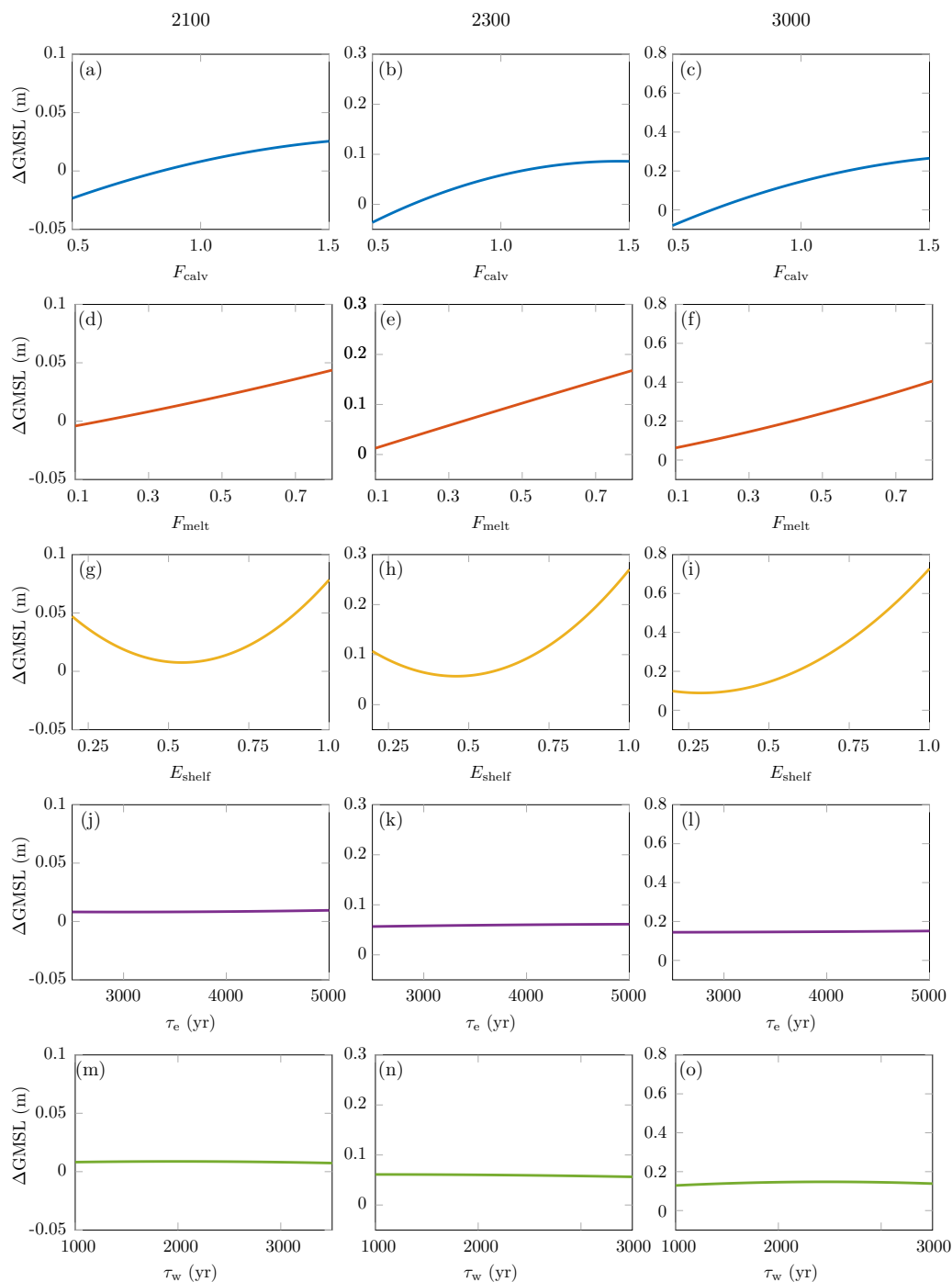
Figure 4. Representation of the parameters-to-projection relationship in RCP 2.6 under the weakly nonlinear sliding law as given by a PC expansion. The PC expansion is shown for each parameter individually with the other parameters are fixed at their nominal value. PC expansions at (**a**, **d**, **g**, **j**, **m**) 2100, (**b**, **e**, **h**, **k**, **n**) 2300 and (**c**, **f**, **i**, **l**, **o**) 3000.
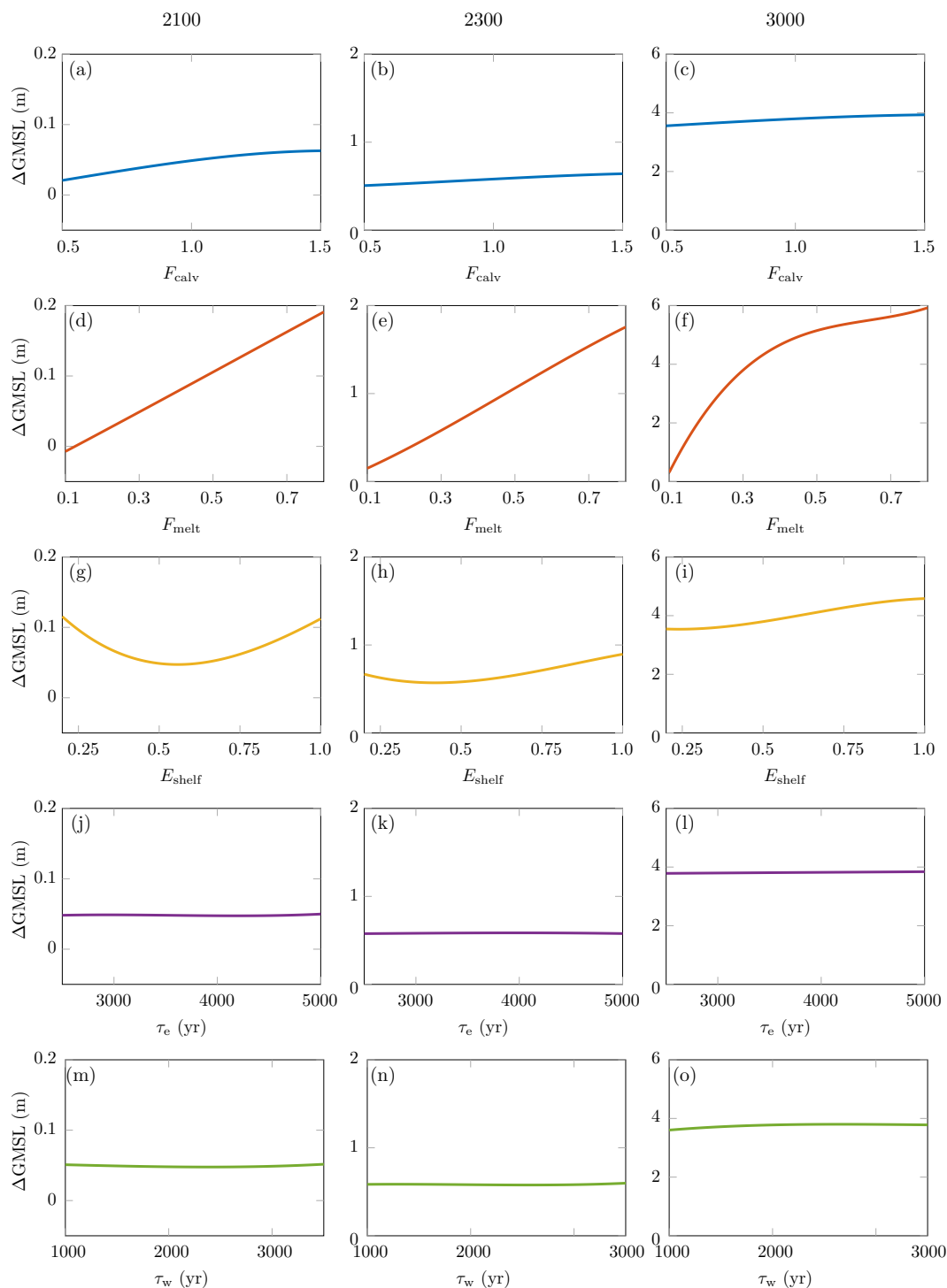
Figure 5. Same as Fig. 4 but in RCP 8.5.

(a)

(b)

(c)
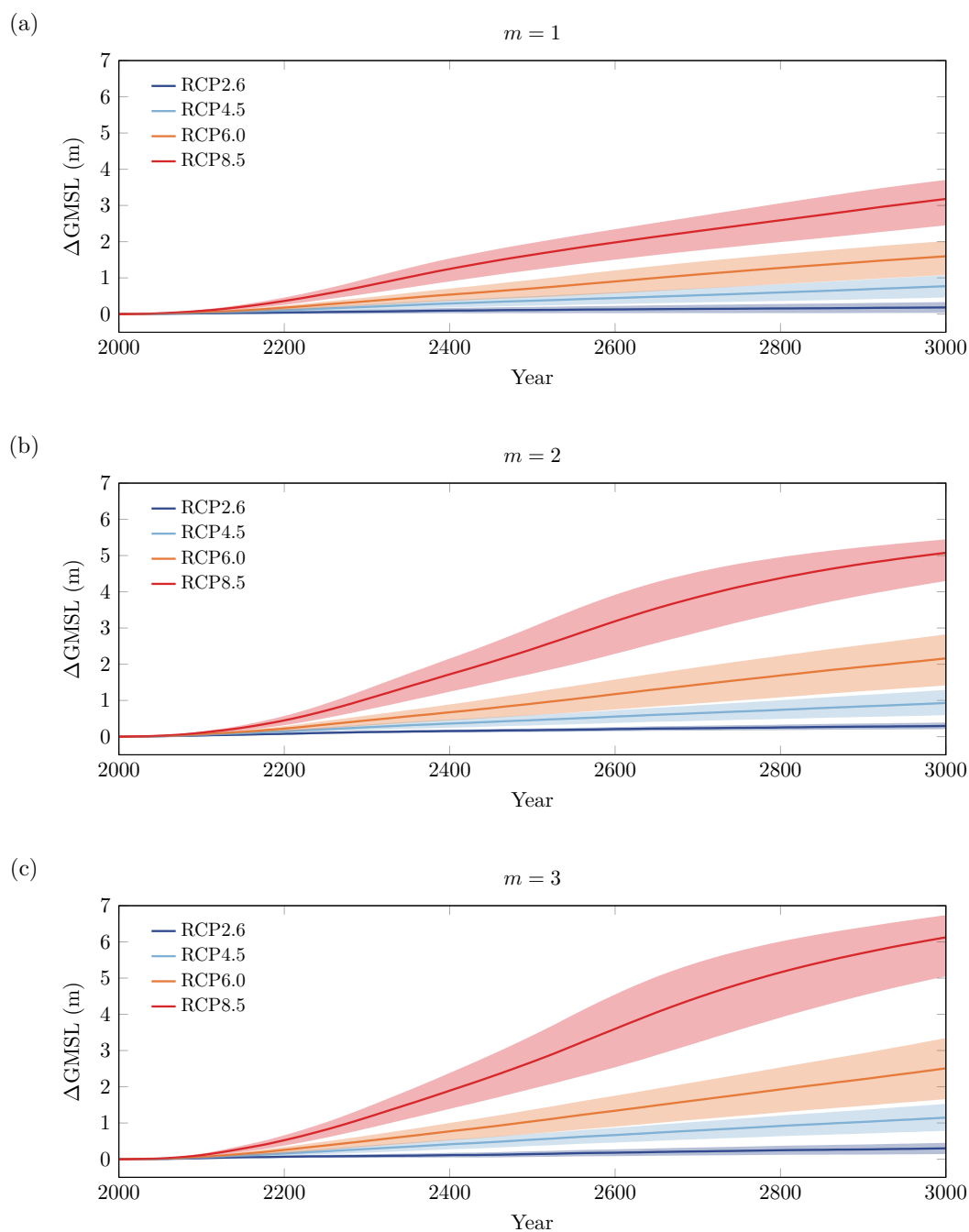
Figure 6. AIS contribution to sea-level rise. (**a**) Viscous sliding law, (**b**) weakly nonlinear sliding law and (**c**) strongly nonlinear sliding law. Solid lines are the median projections and the shaded areas are the 33–66 % probability intervals that represent the parametric uncertainty in the model.
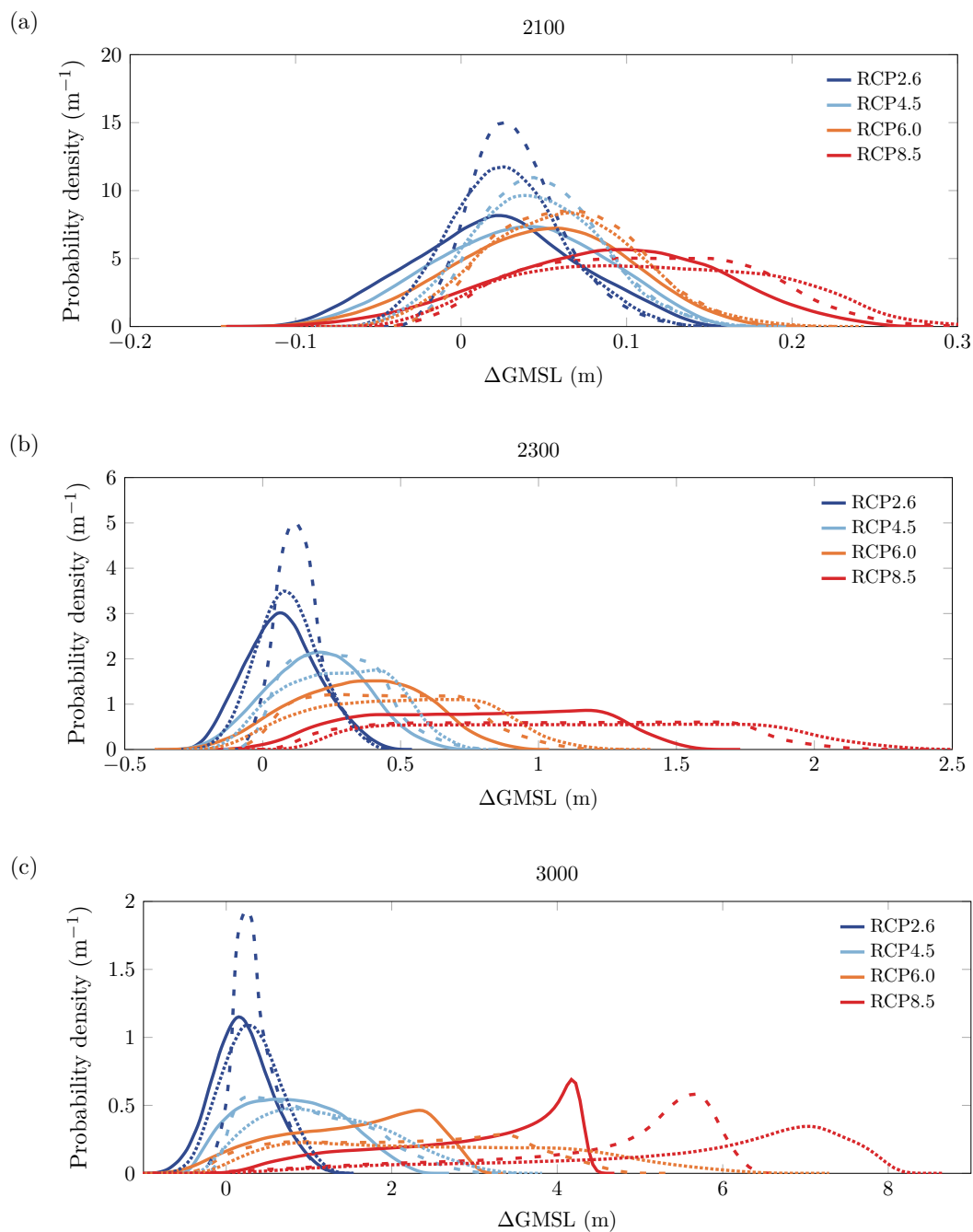
Figure 7. Probability density functions for the AIS contribution to sea-level rise at (**a**) 2100, (**b**) 2300 and (**c**) 3000 under the viscous sliding law (solid lines), the weakly nonlinear sliding law (dashed lines) and the strongly nonlinear sliding law (dotted lines).

(a)

(b)

(c)
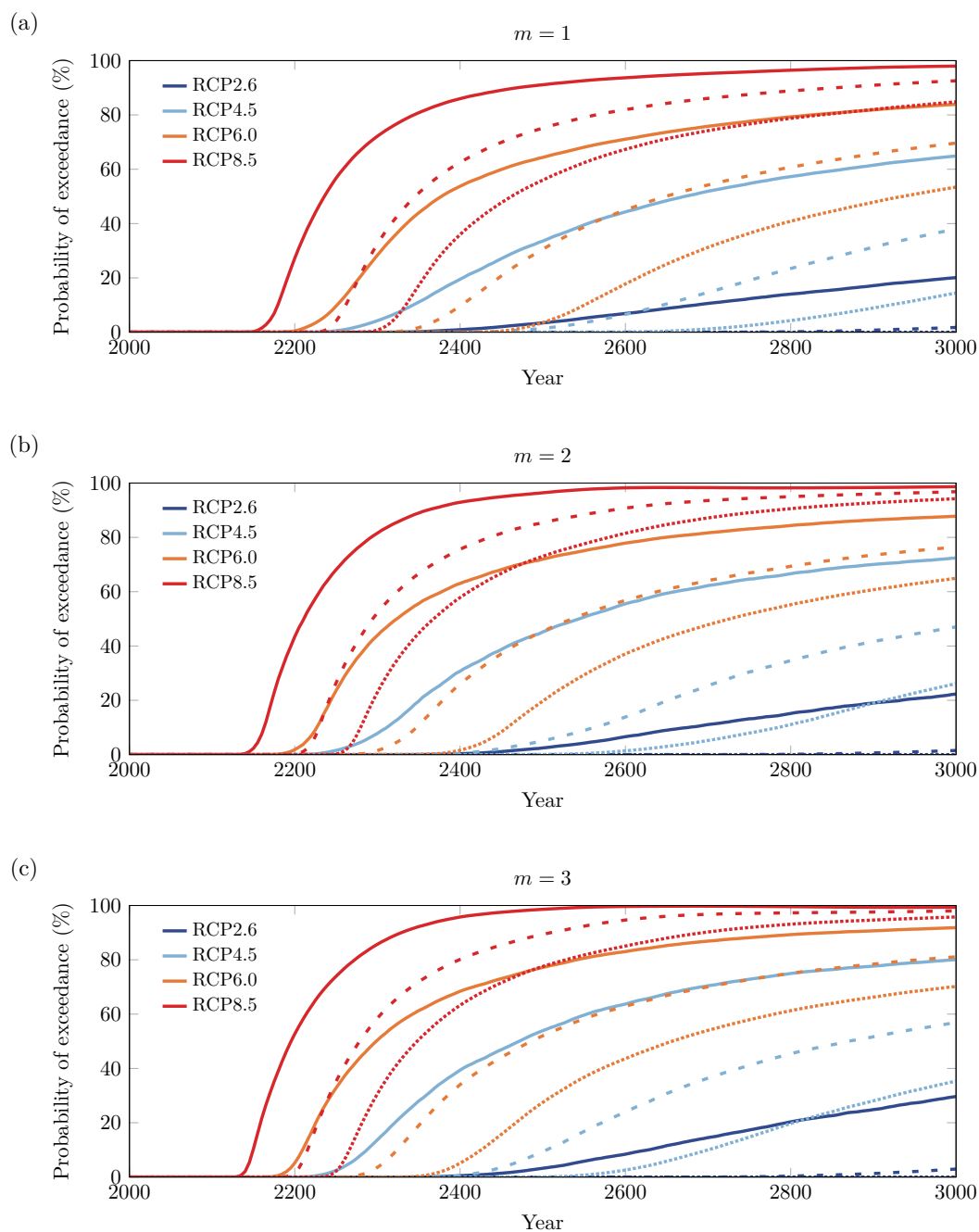
Figure 8. Probability of exceeding some characteristic threshold sea-level rise values as a function of time, evaluated from the complementary cumulative distribution functions of the probability density functions for ΔGMSL. Probability of exceedance under (**a**) the viscous sliding law, (**b**) the weakly nonlinear sliding law and (**c**) the strongly nonlinear sliding law. Solid lines correspond to a threshold value of 0.5 m, dashed lines to a threshold value of 1 m and dotted lines to a threshold value of 1.5 m.
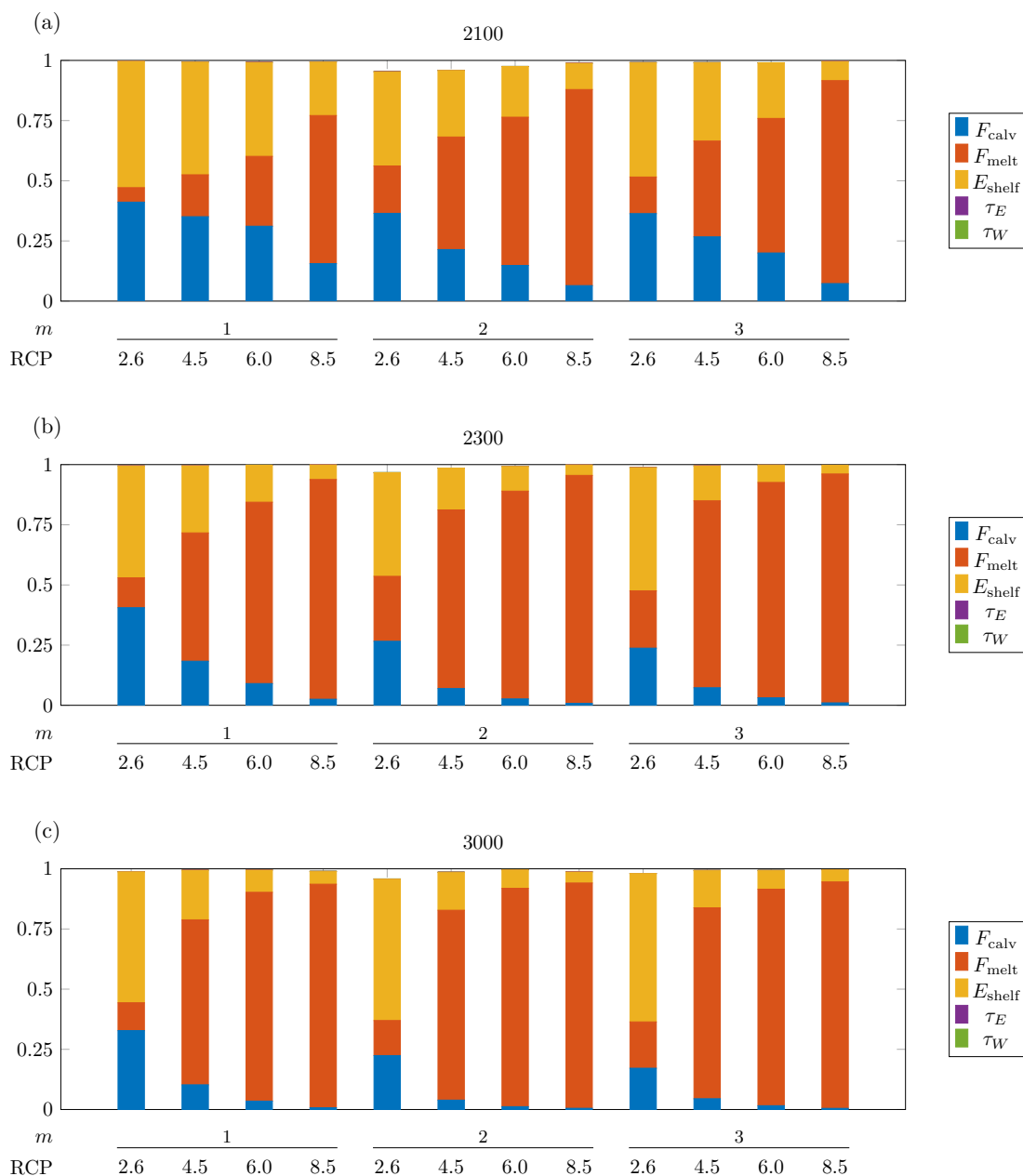
Figure 9. Sobol sensitivity indices for the AIS contribution to sea-level rise in different RCP scenarios and under different sliding laws. Sobol indices at (**a**) 2100, (**b**) 2300 and (**c**) 3000. The gap between the height of a bar and the unit value represents the interaction index.
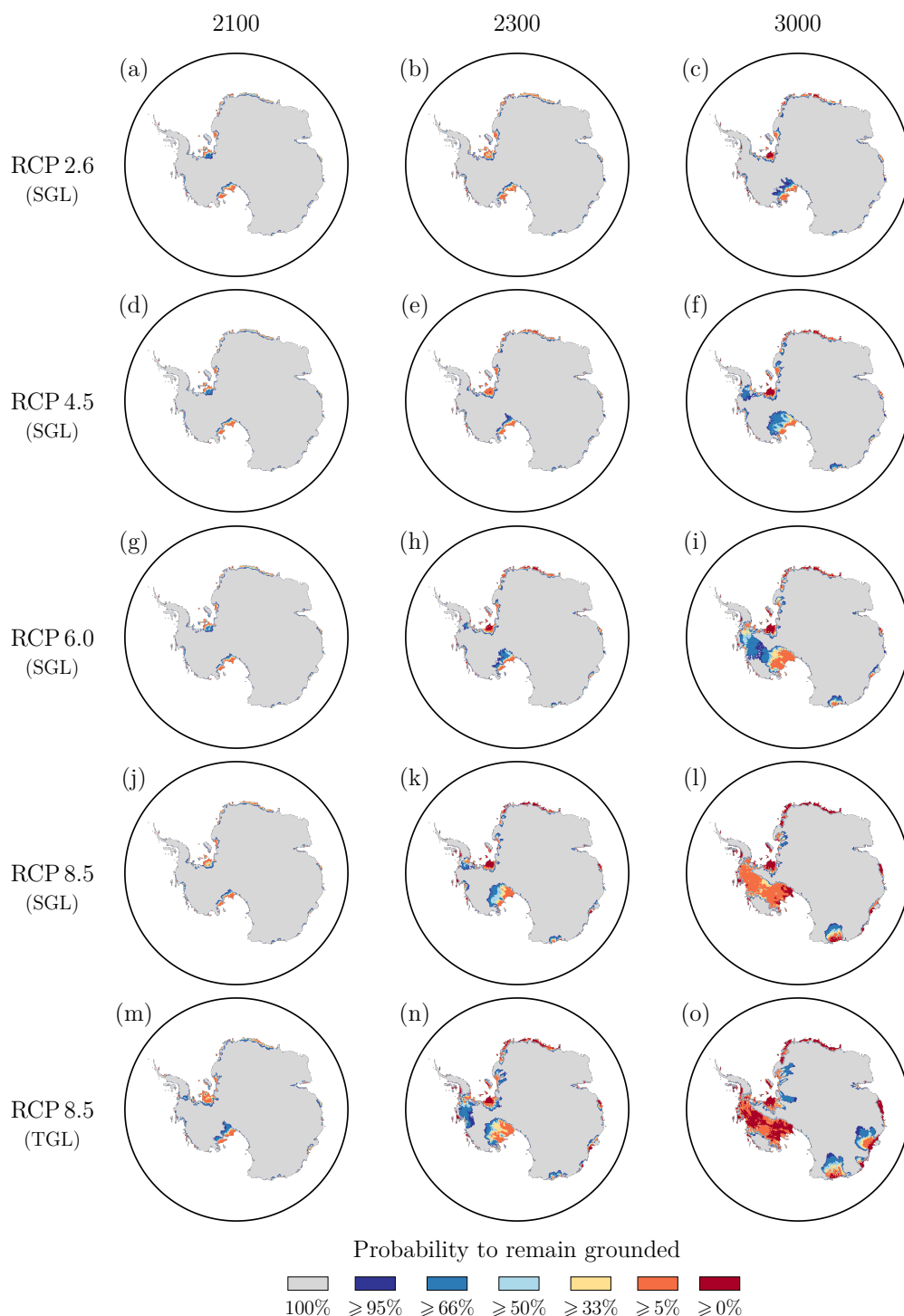
Figure 10. Confidence regions for grounded under the weakly nonlinear sliding law. Confidence regions are shown at (**a**, **d**, **g**, **j,m**) 2100, (**b**, **e**, **h**, **k,n**) 2300 and (**c**, **f**, **i**, **l,o**) 3000. Results under (**a–l**) the SGL parameterisation and (**m–o**) the TGL parameterisation.
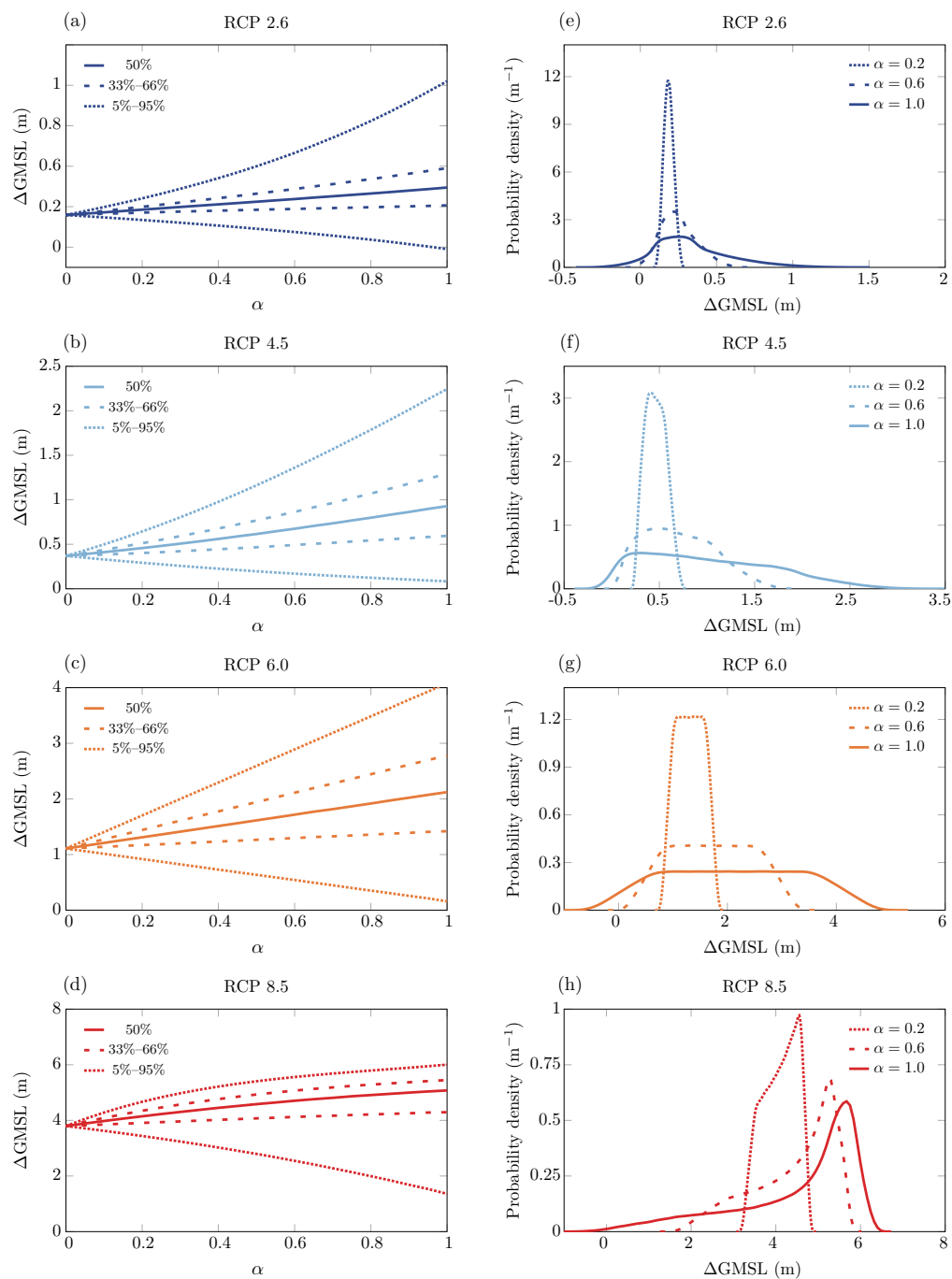
Figure 11. Robustness of probabilistic projections with respect to the scaling factor α. Median projections and their 33–66 % and 5–95 % probability intervals by 3000 under for the weakly nonlinear sliding law in (**a**) RCP 2.6, (**b**) RCP 4.5, (**c**) RCP 6.0 and (**d**) RCP 8.5. Probability density functions for $\alpha = 0.2$ (dotted lines), $\alpha = 0.2$ (dashed lines) and $\alpha = 1$ (solid lines) in (**e**) RCP 2.6, (**f**) RCP 4.5, (**g**) RCP 6.0 and (**h**) RCP 8.5.
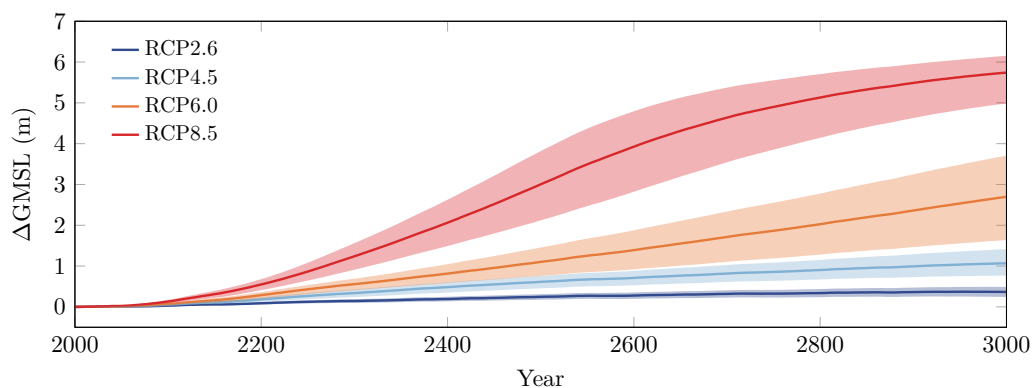
Figure 12. Same as Fig. 6 but under Weertman's sliding law with exponent $m = 5$.
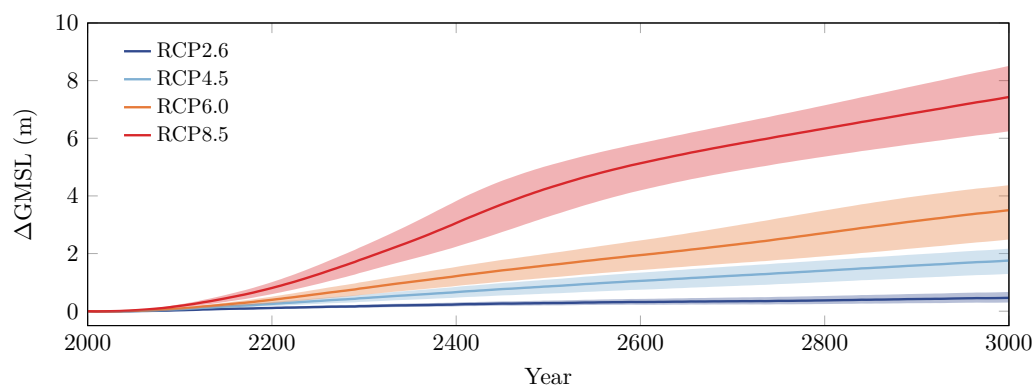
Figure 13. Same as Fig. 6 but under the TGL parameterisation and the weakly nonlinear sliding law.
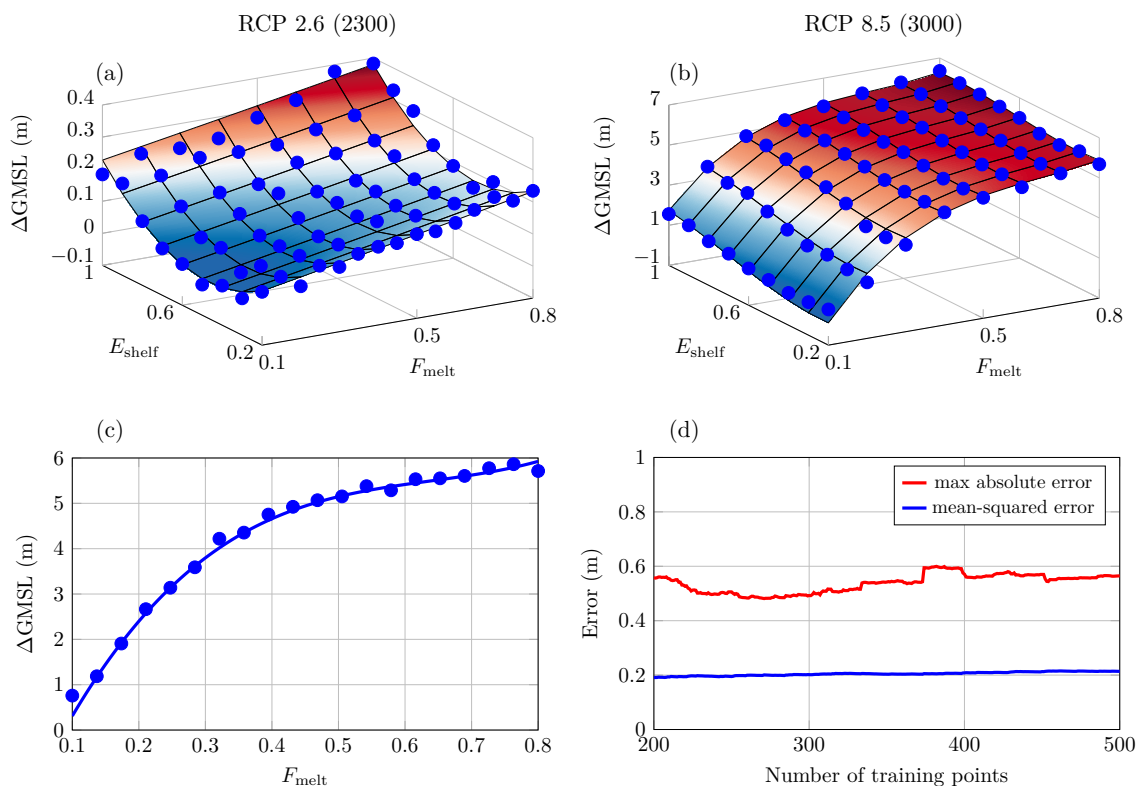
Figure A1. Validation tests for the PC expansion. (**a**) Cross-validation for the PC approximation in Fig. S1d and (**b**) cross-validation for the PC approximation in Fig. S1b. The surface represents the PC approximation of the response of the ice-sheet model and the blue dots are the exact response of the ice-sheet model at the test points. (**c**) Cross-validation for the PC approximation in Fig. 5f showing the presence of noisy results. (**d**) Convergence test in RCP 8.5 at time 3000 based on the number of samples used to build the emulator.